

The Cosmic-Ray Composition between 2 PeV and 2 EeV Observed with the TALE Detector in Monocular Mode

```
R. U. Abbasi<sup>1</sup>, M. Abe<sup>2</sup>, T. Abu-Zayyad<sup>1,3</sup>, M. Allen<sup>3</sup>, Y. Arai<sup>4</sup>, E. Barcikowski<sup>3</sup>, J. W. Belz<sup>3</sup>, D. R. Bergman<sup>3</sup>,
S. A. Blake<sup>3</sup>, R. Cady<sup>3</sup>, B. G. Cheon<sup>5</sup>, J. Chiba<sup>6</sup>, M. Chikawa<sup>7</sup>, T. Fujii<sup>8</sup>, K. Fujisue<sup>7</sup>, K. Fujita<sup>4</sup>, R. Fujiwara<sup>4</sup>, M. Fukushima<sup>7,9</sup>, R. Fukushima<sup>4</sup>, G. Furlich<sup>3</sup>, W. Hanlon<sup>3</sup>, M. Hayashi<sup>10</sup>, N. Hayashida<sup>11</sup>, K. Hibino<sup>11</sup>, R. Higuchi<sup>7</sup>, K. Honda<sup>12</sup>, D. Ikeda<sup>11</sup>, T. Inadomi<sup>13</sup>, N. Inoue<sup>2</sup>, T. Ishii<sup>12</sup>, H. Ito<sup>14</sup>, D. Ivanov<sup>3</sup>, H. Iwakura<sup>13</sup>, H. M. Jeong<sup>15</sup>, S. Jeong<sup>15</sup>, C. C. H. Jui<sup>3</sup>, K. Kadota<sup>16</sup>, F. K. Line and J. R. K. Lin
F. Kakimoto<sup>11</sup>, O. Kalashev<sup>17</sup>, K. Kasahara<sup>18</sup>, S. Kasami<sup>19</sup>, H. Kawai<sup>20</sup>, S. Kawakami<sup>4</sup>, S. Kawana<sup>2</sup>, K. Kawata<sup>7</sup>, E. Kido<sup>14</sup>, H. B. Kim<sup>5</sup>, J. H. Kim<sup>3</sup>, J. H. Kim<sup>3</sup>, M. H. Kim<sup>15</sup>, S. W. Kim<sup>15</sup>, Y. Kimura<sup>4</sup>, S. Kishigami<sup>4</sup>, V. Kuzmin<sup>17,36</sup>, M. Kuznetsov<sup>17,21</sup>, Y. J. Kwon<sup>22</sup>, K. H. Lee<sup>15</sup>, B. Lubsandorzhiev<sup>17</sup>, J. P. Lundquist<sup>3</sup>, K. Machida<sup>12</sup>, H. Matsumiya<sup>4</sup>,
                 T. Matsuyama<sup>4</sup>, J. N. Matthews<sup>3</sup>, R. Mayta<sup>4</sup>, M. Minamino<sup>4</sup>, K. Mukai<sup>12</sup>, I. Myers<sup>3</sup>, S. Nagataki<sup>14</sup>, K. Nakai<sup>4</sup>,
R. Nakamura<sup>13</sup>, T. Nakamura<sup>23</sup>, Y. Nakamura<sup>13</sup>, T. Nonaka<sup>7</sup>, H. Oda<sup>4</sup>, S. Ogio<sup>4,24</sup>, M. Ohnishi<sup>7</sup>, H. Ohoka<sup>7</sup>, Y. Oku<sup>19</sup>, T. Okuda<sup>25</sup>, Y. Omura<sup>4</sup>, M. Ono<sup>14</sup>, R. Onogi<sup>4</sup>, A. Oshima<sup>4</sup>, S. Ozawa<sup>26</sup>, I. H. Park<sup>15</sup>, M. S. Pshirkov<sup>17,27</sup>, J. Remington<sup>3</sup>, D. C. Rodriguez<sup>3</sup>, G. I. Rubtsov<sup>17</sup>, D. Ryu<sup>28</sup>, H. Sagawa<sup>7</sup>, R. Sahara<sup>4</sup>, Y. Saito<sup>13</sup>, N. Sakaki<sup>7</sup>, T. Sako<sup>7</sup>, N. Sakurai<sup>4</sup>, K. Sano<sup>13</sup>, K. Sato<sup>4</sup>, T. Seki<sup>13</sup>, K. Sekino<sup>7</sup>, P. D. Shah<sup>3</sup>, F. Shibata<sup>12</sup>, N. Shibata<sup>19</sup>, T. Shibata<sup>7</sup>, H. Shimodaira<sup>7</sup>, B. K. Shin<sup>28</sup>, H. S. Shin<sup>7</sup>, D. Shinto<sup>19</sup>, J. D. Smith<sup>3</sup>, P. Sokolsky<sup>3</sup>, N. Sone<sup>13</sup>, B. T. Stokes<sup>3</sup>, T. A. Stroman<sup>3</sup>, T. Suzawa<sup>2</sup>, Y. Takagi<sup>4</sup>, Y. Takahashi<sup>4</sup>, M. Takamura<sup>6</sup>, M. Takeda<sup>7</sup>, R. Takeishi<sup>7</sup>, A. Taketa<sup>29</sup>, M. Takita<sup>7</sup>, Y. Tameda<sup>19</sup>, H. Tanaka<sup>4</sup>, K. Tanaka<sup>30</sup>, M. Tanaka<sup>31</sup>, Y. Tanawa<sup>4</sup>, S. R. Thomas<sup>30</sup>, G. R. Thomas<sup>31</sup>, R. Tinyakaya<sup>17,21</sup>, L. Thankay<sup>17</sup>, H. Talawa<sup>32</sup>, T. Tawaia<sup>13</sup>, M. Tanaka<sup>31</sup>, Y. Tanawa<sup>4</sup>, S. R. Thomas<sup>30</sup>, G. R. Thomas<sup>31</sup>, R. Tinyakaya<sup>17,21</sup>, L. Thankay<sup>17</sup>, H. Talawa<sup>32</sup>, T. Tawaia<sup>13</sup>,
      M. Tanaka<sup>31</sup>, Y. Tanoue<sup>4</sup>, S. B. Thomas<sup>3</sup>, G. B. Thomson<sup>3</sup>, P. Tinyakov<sup>17,21</sup>, I. Tkachev<sup>17</sup>, H. Tokuno<sup>32</sup>, T. Tomida<sup>13</sup>,
         S. Troitsky<sup>17</sup>, R. Tsuda<sup>4</sup>, Y. Tsunesada<sup>4,24</sup>, Y. Uchihori<sup>33</sup>, S. Udo<sup>11</sup>, T. Uehama<sup>13</sup>, F. Urban<sup>34</sup>, T. Wong<sup>3</sup>, K. Yada<sup>7</sup>,
                                M. Yamamoto<sup>13</sup>, K. Yamazaki<sup>11</sup>, J. Yang<sup>35</sup>, K. Yashiro<sup>6</sup>, F. Yoshida<sup>19</sup>, Y. Zhezher<sup>7,17</sup>, and Z. Zundel<sup>3</sup>
                                                                                                                           (Telescope Array Collaboration)
                                                                   <sup>1</sup> Department of Physics, Loyola University Chicago, Chicago, IL, USA; tareq@cosmic.utah.edu
                                                                                 The Graduate School of Science and Engineering, Saitama University, Saitama, Japan
                                   <sup>3</sup> High Energy Astrophysics Institute and Department of Physics and Astronomy, University of Utah, Salt Lake City, UT, USA
                                                                                                  Graduate School of Science, Osaka City University, Osaka, Japan
                            <sup>5</sup> Department of Physics and The Research Institute of Natural Science, Hanyang University, Seongdong-gu, Seoul, Republic of Korea
                                                                                           Department of Physics, Tokyo University of Science, Noda, Chiba, Japan
                                                                                 <sup>7</sup> Institute for Cosmic Ray Research, University of Tokyo, Kashiwa, Chiba, Japan
              <sup>8</sup> The Hakubi Center for Advanced Research and Graduate School of Science, Kyoto University, Kitashirakawa-Oiwakecho, Sakyo-ku, Kyoto, Japan
       <sup>9</sup> Kavli Institute for the Physics and Mathematics of the Universe (WPI), Todai Institutes for Advanced Study, University of Tokyo, Kashiwa, Chiba, Japan Information Engineering Graduate School of Science and Technology, Shinshu University, Nagano, Japan
                                                                                        Faculty of Engineering, Kanagawa University, Yokohama, Kanagawa, Japan
                                             <sup>12</sup> Interdisciplinary Graduate School of Medicine and Engineering, University of Yamanashi, Kofu, Yamanashi, Japan
                                           <sup>13</sup> Academic Assembly School of Science and Technology Institute of Engineering, Shinshu University, Nagano, Japan
                                                                                                  Astrophysical Big Bang Laboratory, RIKEN, Wako, Saitama, Japan
                                                                      Department of Physics, Sungkyunkwan University, Jang-an-gu, Suwon, Republic of Korea

16 Department of Physics, Tokyo City University, Setagaya-ku, Tokyo, Japan
                                                                            <sup>17</sup> Institute for Nuclear Research of the Russian Academy of Sciences, Moscow, Russia
                                                        <sup>18</sup> Faculty of Systems Engineering and Science, Shibaura Institute of Technology, Minato-ku, Tokyo, Japan
                            <sup>19</sup> Department of Engineering Science, Faculty of Engineering, Osaka Electro-Communication University, Neyagawa-shi, Osaka, Japan

<sup>20</sup> Department of Physics, Chiba University, Chiba, Japan
                                                                               <sup>21</sup> Service de Physique Théorique, Université Libre de Bruxelles, Brussels, Belgium
                                                                           Department of Physics, Yonsei University, Seodaemun-gu, Seoul, Republic of Korea Faculty of Science, Kochi University, Kochi, Japan
                                                        Nambu Yoichiro Institute of Theoretical and Experimental Physics, Osaka City University, Osaka, Japan
                                                                                     Department of Physical Sciences, Ritsumeikan University, Kusatsu, Shiga, Japan
                     <sup>26</sup> Quantum ICT Advanced Development Center, National Institute for Information and Communications Technology, Koganei, Tokyo, Japan
                                                                      Sternberg Astronomical Institute, Moscow M.V. Lomonosov State University, Moscow, Russia
                 Department of Physics, School of Natural Sciences, Ulsan National Institute of Science and Technology, UNIST-gil, Ulsan, Republic of Korea
                                                                                       Earthquake Research Institute, University of Tokyo, Bunkyo-ku, Tokyo, Japan
                                                                         Graduate School of Information Sciences, Hiroshima City University, Hiroshima, Japan
                                                                                              Institute of Particle and Nuclear Studies, KEK, Tsukuba, Ibaraki, Japan
                                                            <sup>32</sup> Graduate School of Science and Engineering, Tokyo Institute of Technology, Meguro, Tokyo, Japan
         33 Department of Research Planning and Promotion, Quantum Medical Science Directorate, National Institutes for Quantum and Radiological Science and
                                                                                                                                         Technology, Chiba, Japan
                                                                              <sup>34</sup> CEICO, Institute of Physics, Czech Academy of Sciences, Prague, Czech Republic
                              <sup>35</sup> Department of Physics and Institute for the Early Universe, Ewha Womans University, Seodaaemun-gu, Seoul, Republic of Korea
                                                    Received 2020 December 18; revised 2021 January 14; accepted 2021 January 15; published 2021 March 16
```

1

³⁶ Deceased.

Abstract

We report on a measurement of the cosmic-ray composition by the Telescope Array Low-energy Extension (TALE) air fluorescence detector (FD). By making use of the Cherenkov light signal in addition to air fluorescence light from cosmic-ray (CR)-induced extensive air showers, the TALE FD can measure the properties of the cosmic rays with energies as low as \sim 2 PeV and exceeding 1 EeV. In this paper, we present results on the measurement of X_{max} distributions of showers observed over this energy range. Data collected over a period of \sim 4 yr were analyzed for this study. The resulting X_{max} distributions are compared to the Monte Carlo (MC) simulated data distributions for primary cosmic rays with varying composition and a four-component fit is performed. The comparison and fit are performed for energy bins, of width 0.1 or 0.2 in $\log_{10}(E/\text{eV})$, spanning the full range of the measured energies. We also examine the mean X_{max} value as a function of energy for cosmic rays with energies greater than $10^{15.8}$ eV. Below $10^{17.3}$ eV, the slope of the mean X_{max} as a function of energy (the elongation rate) for the data is significantly smaller than that of all elements in the models, indicating that the composition is becoming heavier with energy in this energy range. This is consistent with a rigidity-dependent cutoff of events from Galactic sources. Finally, an increase in the X_{max} elongation rate is observed at energies just above 10^{17} eV, indicating another change in the cosmic-ray composition.

Unified Astronomy Thesaurus concepts: Cosmic rays (329); Cosmic ray showers (327); Cosmic ray detectors (325); Particle astrophysics (96)

1. Introduction

The Telescope Array Low-energy Extension (TALE) detector was designed to look for structure in the energy spectrum and associated change in composition of cosmic rays below the "ankle" structure at $10^{18.6}$ eV. A measurement of the cosmic-ray energy spectrum using TALE observations in the energy range between $10^{15.3}$ eV and $10^{18.3}$ eV was published in a recent article (Abbasi et al. 2018a). Here we present our results on the cosmic-ray composition from $10^{15.3}$ eV to $10^{18.3}$ eV. Only the high-elevation telescopes of TALE, observing 31° to 55° , are used in this analysis. See Section 2 for the experimental setup.

Previous observations of cosmic-ray composition for energies greater than 10¹⁸ eV, such as those reported by HiRes (Abbasi et al. 2005), the Telescope Array (TA) (Abbasi et al. 2015), and Auger (Aloisio et al. 2014), all suggest that the transition from Galactic to extragalactic sources occurs at an energy below that of the ankle. This transition is expected to be observable in the form of a composition getting heavier up to a "transition energy" and then becoming lighter at higher energies. Below the transition energy, Galactic sources dominate the observed flux, while above the transition the sources of cosmic rays are mostly extragalactic.

Several observations of the cosmic-ray energy spectrum, including the one using TALE data, indicate the presence of a "knee"-like structure in the 10^{17} decade, i.e., a second knee. A change in the spectral index of the cosmic-ray flux is also expected in the case of transition from Galactic to extragalactic sources. It is therefore logical to expect to see a correlated change in the flux and composition in the transition region. This paper reports on the observation of just such a correlated change.

We describe the detector and data collection in Section 2. We then briefly discuss event selection and event reconstruction procedures in Section 3. In Section 4 we describe the Monte Carlo (MC) simulation, and present the results of MC studies of the event reconstruction performance. Section 5 presents an overview of the procedures for measuring composition. A discussion of the systematic uncertainties is presented in Section 6. The measured composition is shown in Section 7, along with a brief discussion of the measured results. The paper concludes with a summary in Section 8.

As the second paper on TALE data analysis, it is unavoidable that some of the material presented in this paper reproduces material already published in Abbasi et al. (2018a). Furthermore, we refer the reader to that publication for a more detailed description of the TALE detector and data analysis.

2. TALE Detector and Operation

The Telescope Array is an international collaboration with members from Japan, USA, South Korea, Russia, and Belgium. The observatory is located in the West Desert of Utah, about 150 miles southwest of Salt Lake City, and is the largest cosmic-ray detector in the Northern Hemisphere. In operation since 2008, TA consists of 507 scintillator surface detectors (SDs), arranged in a square grid of 1.2 km spacing (Abu-Zayyad et al. 2013a). A total of 38 telescopes are distributed among three fluorescence detector (FD) stations located on the periphery of the SD array (Abu-Zayyad et al. 2012; Tokuno et al. 2012). The FD telescopes observe the airspace above the SD array. TA is the direct successor to both the Akeno Giant Air Shower Array (AGASA) and the High Resolution Fly's Eye (HiRes) experiments (Teshima et al. 1986; Sokolsky 2011). Telescope Array incorporates both the scintillation counter technique of AGASA and the air fluorescence measurements of HiRes. The goal of the Telescope Array is to clarify the origin and nature of ultrahigh-energy cosmic rays (UHECRs) and the related extremely high-energy phenomena in the universe. The previous measurements of the energy spectrum, composition, and anisotropy in the arrival direction distribution for energies above 10^{18.2} eV have been published (Abu-Zayyad et al. 2013b; Abbasi et al. 2014, 2015).

A TALE fluorescence detector (Thomson et al. 2011) began operation in 2013 at the northern FD station (Middle Drum). Ten new TALE telescopes were added to the 14 telescopes that made up the TA FD at the site. All 24 telescopes were refurbished from components previously used by HiRes, and updated with new communications hardware. The original 14 TA FD telescopes came from HiRes-I and were distributed in two "rings" viewing 3° to 31° in elevation. They are instrumented with sample-and-hold electronics. The TALE FD telescopes, added to TA in 2013, came from HiRes-II and view 31° to 59° in elevation, directly above the field of view of

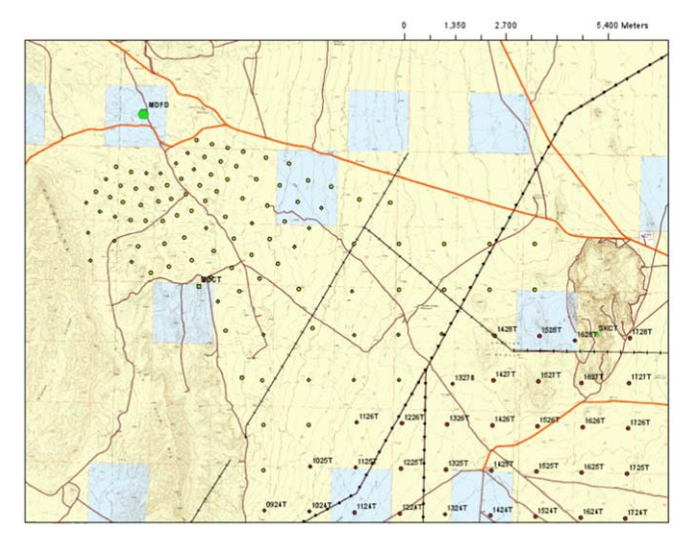


Figure 1. Map of the TALE detector. The locations of the TALE surface detectors are indicated by the yellow circles. The TALE detectors merge with the main Telescope Array surface array at the lower right of the figure. Telescope Array surface detectors are shown by red circles with detector numbers. The location of the TALE FD site can be seen near the top left of the figure indicated on the map by the green hexagon labeled MDFD.

the main TA telescopes. The TALE telescopes are instrumented with FADC electronics.

In addition to the 10 new FD telescopes with high elevation angle, TALE also added 103 new SD counters arranged in a graded spacing array. See Figure 1. Both the TA and TALE telescopes view approximately southeast, over the Telescope Array and TALE SD arrays. This arrangement is illustrated in Figure 2.

The TALE scintillator detectors were added after the telescopes in 2017. Since the telescopes were taking data before the scintillators were deployed, the analysis described in this paper is based only upon observations made by the FD component of TALE.

The TALE FD telescopes were assembled from refurbished HiRes-II telescopes (Boyer et al. 2002). The telescope mirrors are each made from four truncated circular segments, which were assembled into a clover-leaf pattern. The unobscured viewing area of each spherical mirror is approximately $3.7~{\rm m}^2$. The focal plane of the telescope camera consists of $256~(16\times16)$ hexagonal photomultiplier tubes (PMTs). The Philips/Photonis XP3062 PMTs are 40 mm (flat-to-flat) where each PMT/pixel views a 1° cone in the sky. The field of view (FOV) of each camera is about 16° in azimuth by 14° in elevation.

The TALE telescope electronics consist of a 10 MHz FADC readout system with 8 bit resolution. Analog sums over the rows and columns of pixels, also sampled at 8 bits, allow recovery of saturated PMTs in most cases. The trigger logic of the telescope also uses the digitized summed signals. Systems for telescope GPS timing, inter-telescope triggers, and communication to a central data acquisition (DAQ) computer use new hardware that resulted in a significant improvement in throughput over the old HiRes-II system, and are documented in Zundel (2016).

Useful events recorded by the TALE detector appear as tracks for which the observed signal comprises a combination of direct Cherenkov light (CL) and fluorescence light (FL), with some contribution from scattered CL. Contributions of

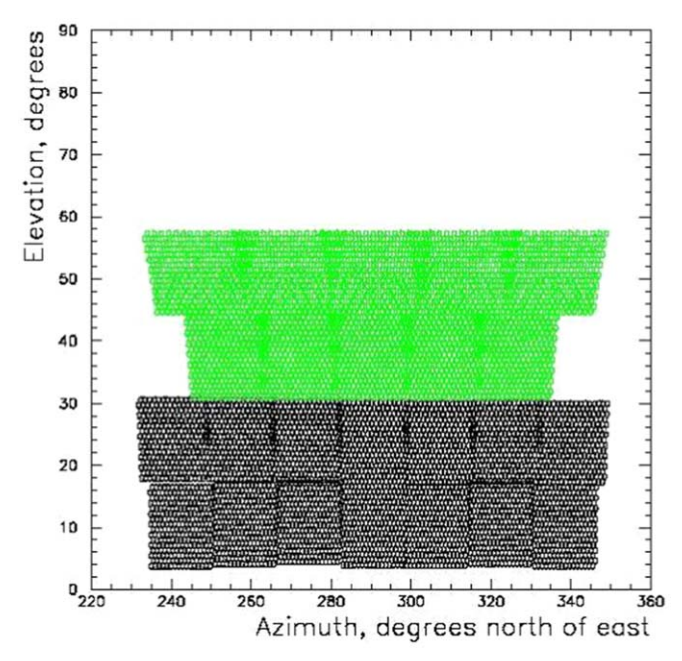


Figure 2. Schematic of TALE/MD telescopes' field of view, showing azimuthal and elevation coverage. Each small hexagon represents the field of view of a single PMT, while the broad box outlines show the field of view of a 256 PMT telescope camera. The view of the 14 TA telescopes is shown in black, while that of the 10 TALE telescopes is shown in green.

light generated by these mechanisms are both proportional to the number of charged particles in the extensive air shower (EAS) at any point along its development. Thus, CL signals can be analyzed in a manner analogous to that for FL to determine the energy of the cosmic ray, as well as to determine the depth of shower maximum $(X_{\rm max})$, which is related to the composition of the primary particle.

There are some important differences between the CL and FL measurements. First, FL is emitted isotropically along the shower from the particles. In contrast, the CL is strongly peaked in the forward direction along the shower axis. As a result, CL falls off rapidly as the incident angle of the shower to the detector increases. In addition, the CL also accumulates along the shower track and therefore increases in overall intensity as the shower develops. Both types of light also undergo scattering in the atmosphere, from both air molecules (Rayleigh scattering) and particulate aerosols.

At the lowest energies observable by TALE, events are dominated by CL. At higher energies, however, the FD becomes more sensitive to the isotropically emitted FL. In the energy region between $10^{16.5}$ eV and $10^{17.5}$ eV, the shower events are typically recorded with a mix of both CL and FL. Based upon our experience with calculation of the TALE energy spectrum, we concluded that a composition analysis, which requires accurate reconstruction of the shower geometry, should be restricted to use only those events with a significant contribution of direct CL. Therefore, we restrict our analysis to events with direct CL > 35% of the total recorded signal; see Section 3 and Table 2 of Abbasi et al. (2018a).

TALE FD data collected between 2014 June and 2018 November are included in this analysis. This data set includes, as a subset, the data set used for the energy spectrum paper (Abbasi et al. 2018a). However, this data set is more than double the size of the original spectrum data set. The criterion used to determine good weather is the same as in the

original analysis. The total detector on-time with good weather in this period is \sim 2700 hr.

3. Event Processing and Reconstruction

Most TALE FD data events are the result of noise triggers or very low-energy air showers that cannot be reliably used for physics analysis. An event processing chain is used that filters out low-quality events. After filtering, the remaining events are subjected to full shower reconstruction, which includes the determination of shower geometry, energy, and the depth of shower maximum.

The event reconstruction procedure consists of the following main steps: First, the shower-detector plane (SDP) is reconstructed from the pattern and pointing direction of the triggered PMT pixels.

Next, the arrival time of light at the detector (in each pixel) is fit as a function of the viewing angle of the pixel in the SDP:

$$t_i = t_0 + \frac{R_p}{c} \tan\left(\frac{\pi - \psi - \chi_i}{2}\right),\tag{1}$$

where R_p is the impact parameter or distance of closest approach from the detector to the shower track, ψ is the incline angle of the track within the SDP, t_0 is a time offset, and χ_i is the viewing angle of the *i*th pixel.

The PMT signal is then fit to the light profile expected for a given energy and shower X_{\max} according to the Gaisser–Hillas parameterization:

$$N(x) = N_{\text{max}} \left(\frac{x - X_0}{X_{\text{max}} - X_0} \right)^{(X_{\text{max}} - X_0)/\lambda} \exp\left(\frac{X_{\text{max}} - x}{\lambda} \right). \tag{2}$$

The parameterization gives the number of charged particles, N, at atmospheric depth x along the shower track. N_{max} , X_{max} , X_0 , and λ are parameters. Here, N_{max} is the number of shower particles at the point of maximum shower development, X_{max} . X_0 is a fit parameter roughly indicating the starting depth of the shower and $\lambda = 70 \text{ g cm}^{-2}$. In combination with X_0 , λ sets the width of the shower profile curve. The fit produces two numbers of interest: X_{max} , the depth of shower maximum development, and the shower's calorimetric energy. The calculation of the total shower energy follows from the fit results, as explained below.

The profile-constrained geometry fit (PCGF) (Abu-Zayyad 2000) was used to reconstruct these TALE data. When applied to TALE events with a significant CL signal, we found that the PCGF results in very good geometric resolution (Abbasi et al. 2018a). Based upon MC studies, we determined that a direct CL fraction of at least 35% was optimal for maintaining good geometric reconstruction and at the same time increasing event statistics at higher energies, approaching $10^{18}\,\mathrm{eV}$.

The PCGF reconstruction produces an estimate for the shower calorimetric energy. To obtain the total shower energy, i.e., the primary CR particle energy, a missing-energy correction is applied. This correction is composition-dependent, and is therefore applied after the best-fit composition parameters have been determined. We refer to the primary mixture obtained from fitting TALE data as "TXF", for TALE X_{max} distributions fits; see Section 5. Post-reconstruction, event selection criteria (quality cuts) are summarized in Table 1.

Table 1
Quality Cuts Applied to Events Used for the Composition Measurement

Variable	CL
Angular track-length [deg]	<i>trk</i> > 6°.1
Inverse angular speed [μ s deg ⁻¹]	$0.014 < 1/\omega < 0.1$
Shower impact parameter [km]	$0.4 < R_p < 5.0$
Shower zenith angle [deg]	$28^{\circ} < \theta < 65^{\circ}$
Shower X_{max} [g cm ⁻²]	$435 < X_{\text{max}} < 920$
Estimated fit error on energy	$\delta E/E < 0.6$
Estimated fit error on X_{max} [g cm ⁻²]	$\delta X_{\rm max} < 200$
Timing fit χ^2/dof	$\chi^{2}_{\rm tim} < 4.5$
Profile fit χ^2/dof	$\chi^2_{\rm pfl} < 12$

Note. Events meeting these conditions remain in the analysis.

4. Simulation

We use Monte Carlo simulations to study the detector efficiency and reconstruction resolution. Two sets of simulations were generated for this analysis using different hadronic interaction models. The first set of simulations was based upon QGSJetII-03 (Ostapchenko 2007) and a second set was based upon EPOS-LHC (Pierog et al. 2015). QGSjetII-03 is the model that was previously used for measuring the TALE energy spectrum (Abbasi et al. 2018a), while the EPOS-LHC model is a "post-LHC" model, i.e., a hadronic interaction model that has been updated with LHC data.

The full processing of a set of simulations is time-consuming. This made it unfeasible for us to perform the full analysis using other, post-LHC, hadronic interaction models, such as QGSJetII-04 (Ostapchenko 2011). We do note, however, that a comparison of CONEX (Bergmann et al. 2007) simulations in the energy range of interest for this publication shows that the air shower's $\langle X_{\rm max} \rangle$ predictions of QGSJetII-03 are within 5.0 g cm⁻² of the QGSJetII-04 model for all of the four primaries used in this analysis, as demonstrated in Figure 3.

For both sets of simulations, with the QGSjetII-03 and EPOS-LHC hadronic interaction models, a uniform mixture of four primaries {H, He, N, Fe} was simulated for the energy range of 10^{15} – $10^{18.5}$ eV. The showers were thrown following a power-law flux with a spectral index of -2.92. The MC shower events were then re-weighted to fit a broken power-law spectrum consistent with the measurement of the TALE energy spectrum.

A detailed simulation of the TALE detector response to cosmic-ray-generated air showers is performed. For each hadronic interaction model, a library of air showers generated using the CONEX package is used as input to the detector MC. Light production by shower particles and light propagation to the detector, including accurate determination of photon arrival time, are performed. This is followed by a detailed simulation of the detector optics and development of the electronics signal, and finally by simulation of the detector trigger and event-forming logic. A more complete discussion of the simulation can be found in Section 4 of Abbasi et al. (2018a).

The MC is generated for each data collection time interval in which the TALE telescope station was operated. Nightly atmospheric conditions (GDAS ARL-NOAA 2004 database with three-hour intervals) and information on nightly detector calibration are incorporated into the simulation. Each MC data set is about twice size of the actual data set.

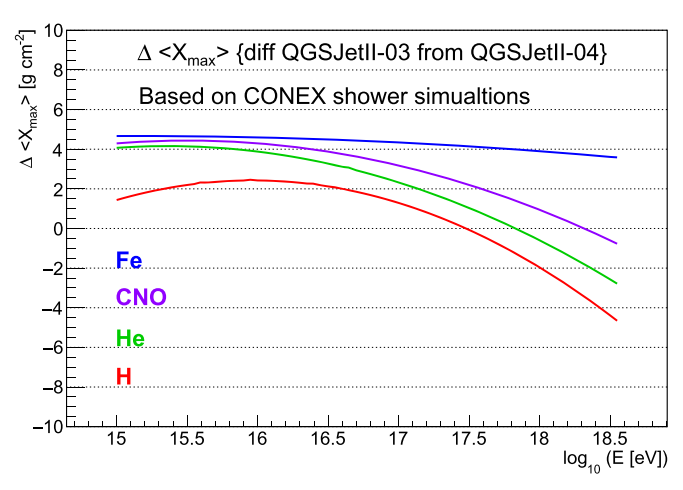


Figure 3. Difference in mean $X_{\rm max}$ predictions for the QGSjetII-03 and QGSjetII-04 hadronic interaction models. The difference between the mean shower maximum in showers generated using QGSjetII-03 and that in showers using QGSJetII-04 is shown as a function of energy for four different cosmic-ray primaries: H, He, N (CNO), and Fe. The shower simulations were generated using CONEX.

Simulated MC showers pass through the same event selection criteria as the real data and they are reconstructed using the same program/procedure. A missing-energy correction is applied to both the reconstructed data and MC showers based on the same assumption of composition, with the correction for each primary type and energy being estimated from the CONEX-generated showers.

Here, the cosmic-ray composition is described by the fit fractions of the various primaries obtained in this study. The fitting procedure uses the measured calorimetric energy of the showers. After the fit fractions are calculated, this information is incorporated into the analysis scripts to estimate the total shower energy for each event as a weighted average over the four primaries used in the simulations, with the fit fractions as weights.

We next present event reconstruction performance, namely resolution and bias of reconstructed shower parameters. The most relevant shower parameters are:

- 1. the angle in the shower-detector plane, ψ
- 2. the shower impact parameter to the detector, R_p
- 3. the depth of shower maximum, X_{max} , and
- 4. the shower energy, E.

The first set of results is shown for all MC showers, i.e., four primaries. The same number of showers were generated for each primary, but the detection and reconstruction efficiencies are different for each primary and therefore the final number of showers is different. Note that the results shown here use the EPOS-LHC simulation set. The results using the QGSJetII-3 hadronic generator are similar.

Figures 4–7 show the difference between the reconstructed and thrown values of simulated events, i.e., the reconstruction resolution of the shower parameters. In light of the steeply falling number of events with energy, each figure is shown as three separate plots, one per energy decade.

As can be seen from the figures, the reconstruction performance improves with energy. The ψ resolution for the three energy ranges is 1°.1, 0°.83, and 0°.67. The fractional error in the impact parameter, dR_p/R_p , expressed as a percentage is 7.5%, 3.5%, and 2.0%. The $X_{\rm max}$ resolution averaged over the four primaries is 47, 40, and 31 g cm⁻². In all cases, the bias in

the reconstruction is small compared to the resolution. Figure 7 shows the resolutions for the reconstructed energy, dE/E. The energy resolutions are 17%, 11%, and 9% for the three energy bins. For the full range of the data set, we see negligible bias in the reconstructed energy values. Note that the energy estimate here includes the missing-energy correction.

The second set of results is shown for individual CR primaries. Here we only show the $X_{\rm max}$ results (see Figure 8) since this is the only variable that shows any significant variance for the different primaries. The total shower energy will naturally be biased since we use an average missing-energy correction. As can be seen from Figure 8, the $X_{\rm max}$ resolution has similar magnitude and improves with energy for each type of primary. The reconstruction bias, however, shows a dependence on primary type, as can be seen by looking at the means of the distributions in Figure 8. At lower energies, we see that $X_{\rm max}$ is underestimated for the lighter primaries and overestimated for heavier primaries. The difference in bias among the different primaries decreases with energy.

As a further check on the shower reconstruction performance, we tested an alternative simulation procedure for the detector response. We replaced the calculation of shower Cherenkov photons reaching the TALE detector, performed by our usual MC program, with a procedure using CORSIKA with the IACT package (Bernlohr 2008). Photons generated by CORSIKA are "injected" into the simulated detector at the times and into the pixels predicted by the IACT package. This calculation is independent of the one used in the reconstruction and can serve to test the validity of the Cherenkov light modeling used in event reconstruction, as well as to verify our estimates for the shower reconstruction performance. A study using the two detector simulation procedures showed good agreement between the estimates of the detector acceptance (\sim 10%) and reconstruction performance: energy (\sim 5%), $X_{\rm max}$ $(\sim 10 \,\mathrm{g \, cm^{-2}})$, when using identical sets of CORSIKA showers. The same reconstruction procedure was applied to both sets. The reader is referred to Abbasi et al. (2018a) for more details on this study.

5. Composition Analysis

We examine both the mean depth of shower maximum, $\langle X_{\text{max}} \rangle$, and the full X_{max} distribution in order to study the composition of cosmic rays. The mean depth of shower maximum is known to depend upon the type of cosmic-ray primary. Therefore, the change in the mean X_{max} with energy, the *elongation rate*, can be examined for indications of a change in composition, e.g., evolution from a heavy to a light composition or vice versa. Comparison of the mean X_{max} to that of MC showers of different primary types allow for inference of the dominant (if any) primary in the measured flux.

Note that the detector acceptance and the biases in event selection and reconstruction result in a primary mixture in the final data set that is different from the true mixture, arriving at the top of the atmosphere. Therefore, the results can only be interpreted by comparison to MC-generated showers. The reconstructed MC showers are subject to the same biases as the real showers.

The analysis fits the histogram of the full $X_{\rm max}$ distribution of the observed data to the weighted sum of four histograms of reconstructed MC showers, one for each simulated primary type. The result of the fit is a set of weights (fit fractions) that are used to produce a combined MC histogram, as a weighted

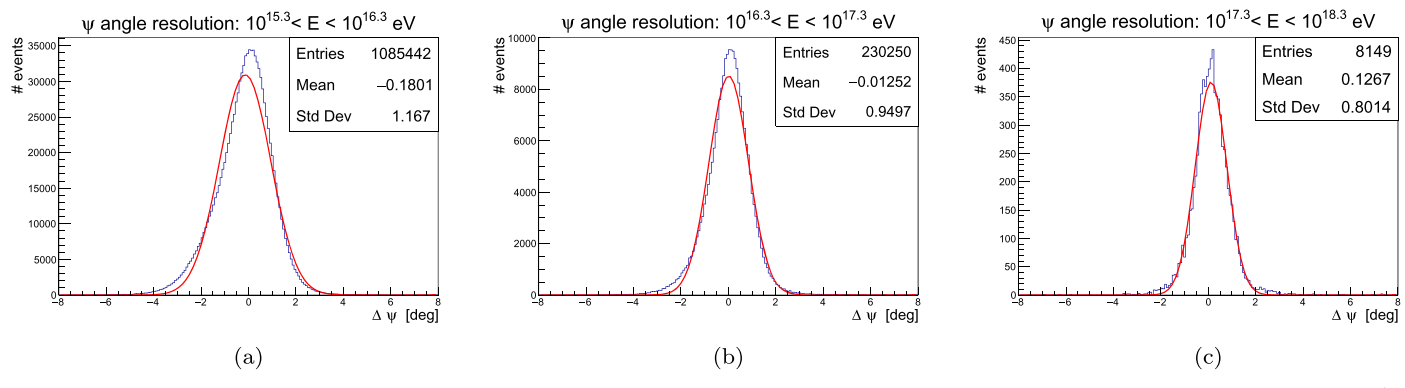


Figure 4. Reconstruction resolution of the shower angle in the shower-detector plane, ψ . The red curve is a Gaussian fit to the distribution of the uncertainty, $\Delta \psi$ [deg]. Distribution statistics are displayed in top right box. The MC uses the EPOS-LHC hadronic generator and a mixed composition, matching the TXF results. From left to right, the histograms show the distribution of the uncertainty, $\Delta \psi$ [deg], for events reconstructed in three energy ranges: $10^{15.3}$ – $10^{16.3}$ eV, $10^{16.3}$ – $10^{17.3}$ eV, and $10^{17.3}$ – $10^{18.3}$ eV. The resolution of the shower angle, ψ , along with the resolution of the impact parameter, R_p , determines the accuracy of the shower track reconstruction.

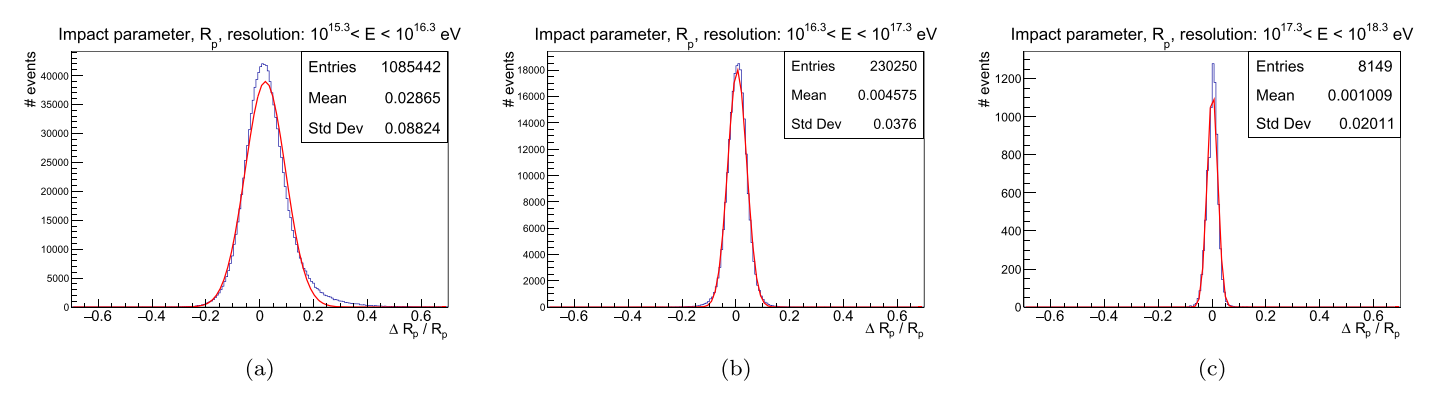


Figure 5. Reconstruction resolution of the shower impact parameter, R_p . The red curve is a Gaussian fit to the distribution of the fractional uncertainty, $\Delta R_p/R_p$. Distribution statistics are displayed in top right box. The MC uses the EPOS-LHC hadronic generator and a mixed composition, matching the TXF results. From left to right, the histograms show the distribution of the fractional uncertainty, $\Delta R_p/R_p$, for events reconstructed in three energy ranges: $10^{15.3}$ – $10^{16.3}$ eV, $10^{16.3}$ – $10^{17.3}$ eV, and $10^{17.3}$ – $10^{18.3}$ eV. As can be seen, the resolution improves significantly with energy.

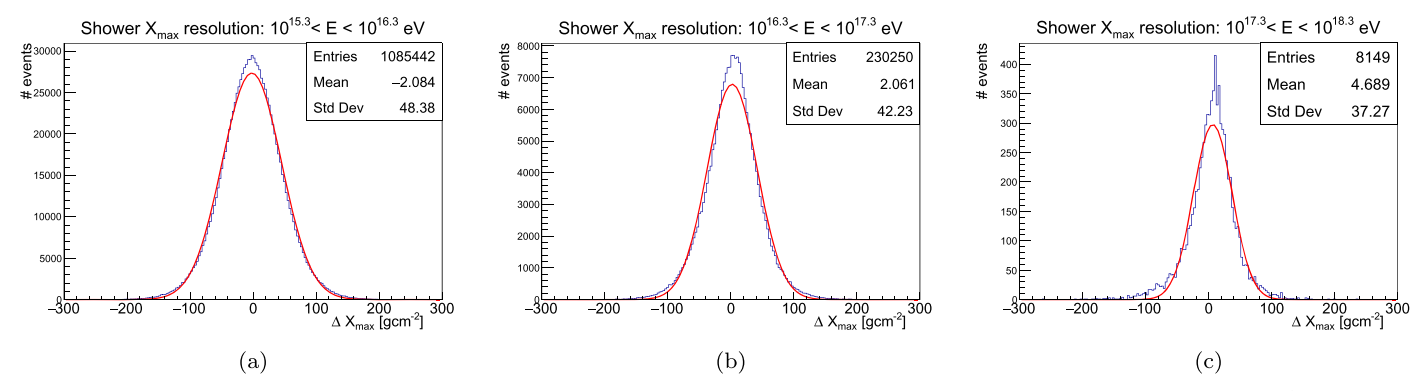


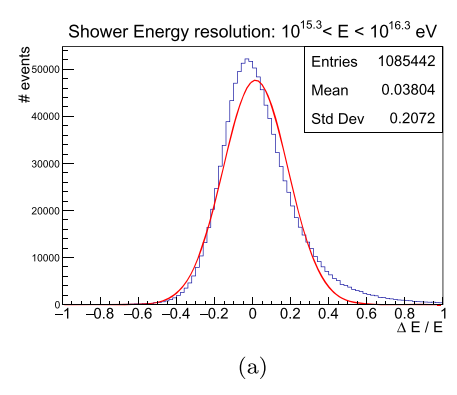
Figure 6. Reconstruction resolution of shower maximum, X_{max} . The red curve is a Gaussian fit to the distribution of the uncertainty, ΔX_{max} [g cm⁻²]. Distribution statistics are displayed in top right box. The MC uses the EPOS-LHC hadronic generator and a mixed composition, matching the TXF results. From left to right, the histograms show the distribution of the uncertainty, ΔX_{max} [g cm⁻²], for events reconstructed in different energy ranges: $10^{15.3}$ – $10^{16.3}$ eV, $10^{16.3}$ – $10^{17.3}$ eV, and $10^{17.3}$ – $10^{18.3}$ eV.

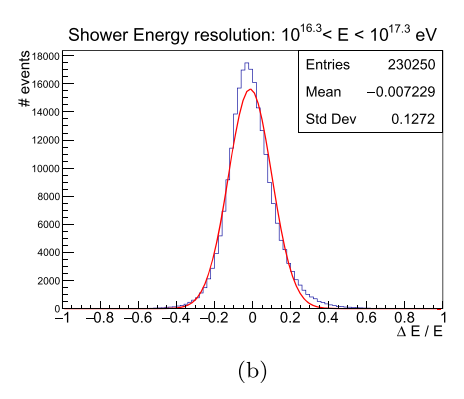
sum of the four primary MC histograms, that best matches the data histogram. The fractions are corrected for the detector acceptance of each primary, using the known MC event counts, to produce fractions that are independent of the detector acceptance.

The fit procedure starts by binning the reconstructed events in energy using a bin size of 0.1 in $\log_{10}(E_{\rm cal}/{\rm eV})$, where $E_{\rm cal}$ is the reconstructed calorimetric shower energy. This is the energy estimate obtained from the fit to the PMT signals, and is independent of primary type. In each energy bin, the data and

MC $X_{\rm max}$ distributions are histogrammed with a bin size of $10~{\rm g~cm^{-2}}$. The fit is performed by calculating a weighted sum of the four MC histograms representing the reconstructed $X_{\rm max}$ distributions of the four primaries (Barlow & Beeston 1993; Filthaut 2002). A "true fraction" is then determined taking into account the relative detection and reconstruction efficiencies for each primary type.

As is well known from shower simulations, there is significant overlap in the X_{max} distributions obtained from different cosmic-ray primary particles with the same energy. A





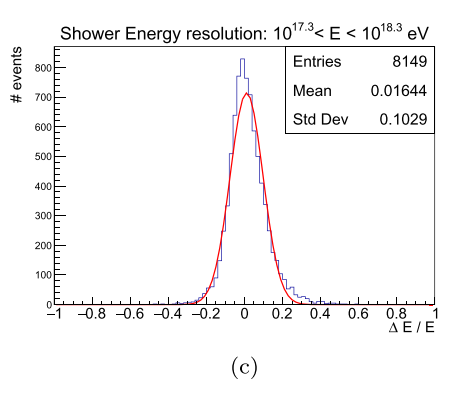


Figure 7. Reconstruction resolution of the shower energy, E. The red curve is a Gaussian fit to the distribution of the fractional uncertainty, $\Delta E/E$. Distribution statistics are displayed in top right box. The MC uses the EPOS-LHC hadronic generator and a mixed composition, matching the TXF results. From left to right, the histograms show the distribution of the fractional uncertainty, $\Delta E/E$, for events reconstructed in three energy ranges: $10^{15.3}$ – $10^{16.3}$ eV, $10^{16.3}$ – $10^{17.3}$ eV, and $10^{17.3}$ – $10^{18.3}$ eV.

practical consequence of this fact is that attempts to fit a measured distribution using MC-generated distributions do not benefit from including many primaries in the fit. On the contrary, the fit becomes unstable, and gives results with highly correlated fit parameters, i.e., primary fractions, making the physical interpretation of the results difficult. For this reason, we chose to use only four primaries for this analysis, namely H, He, N (CNO), and Fe that cover the range of interest. An example of the measured X_{max} distributions, and X_{max} distributions reconstructed from MC primaries in the same energy bin, $15.2 < \log_{10}(E_{cal}/eV) < 15.3$, is shown in Figure 9. We find that that the choice of four primaries is sufficient to provide a good fit to the data at all energies. This is shown in Figure 10 for the same energy bin. The figure also shows the reconstructed X_{max} distribution that results from using the H4a (Gaisser 2012) composition model as input to the TALE detector simulation.

6. Systematic Uncertainties

The main sources of systematic uncertainties on the $\langle X_{\text{max}} \rangle$ measurement are the energy scale uncertainty and possible uncertainty in the detector acceptance calculations in the MC. The main source of uncertainty in the measurement of cosmic-ray composition, i.e., estimates of primary fractions, comes from the selection of the hadronic model used in the shower simulations.

The total energy scale uncertainty of the TALE detector was estimated to be $\pm 15\%$, including a $\pm 10\%$ contribution from the shower missing-energy correction (Abbasi et al. 2018a). This implies that the uncertainty on the reconstructed shower calorimetric energy is $\sim\!10\%$. To estimate the systematic uncertainty on the fit to the primary fractions and quantities derived from them, we propagate the uncertainty in the calorimetric energy, as explained below.

Systematic uncertainties due to detector acceptance effects are investigated below; however, they are not folded into the final systematic uncertainty. This is due to the fact that some of contributions are small enough to be ignored, while others are contained within the calorimetric energy uncertainty and are therefore already accounted for.

The choice of hadronic model determines the predicted $X_{\rm max}$ distribution for each of the primary particles that is used to fit the data $X_{\rm max}$ distributions. To a first approximation, we can consider the differences in the predictions of each hadronic model for the mean value of $X_{\rm max}$ of each primary as a measure of the

systematic uncertainty introduced by the choice of a particular model. An examination of the shower simulations using various post-LHC models (Pierog 2018) has shown that the predictions of the different models for the mean $X_{\rm max}$ lie in an interval of about $20\,{\rm g\,cm^{-2}}$, with EPOS-LHC producing results in the middle of those predicted by QGSJetII-04 and Sybil2.3-c (Engel et al. 2017). We therefore estimate the uncertainty on $\langle X_{\rm max} \rangle$ of simulated CR primaries to be $\pm 10\,{\rm g\,cm^{-2}}$ around those used in our EPOS-LHC MC set.

The data analysis was also performed using the QGSJetII-03 model, producing an equivalent set of results that can be compared to the results using EPOS-LHC. A comparison of the results using the two models includes the effects not only of differences in the $\langle X_{\rm max} \rangle$ but also of the full $X_{\rm max}$ distributions. In addition, the comparison introduces a shift in the energy scale due to the different missing-energy correction.

The systematic uncertainty on the $\langle X_{\rm max} \rangle$ measurements was calculated by shifting the (total) energy of the reconstructed event by $\pm 15\%$, while also shifting its $X_{\rm max}$ by $\pm 10\,{\rm g\,cm^{-2}}$. The \pm sign in both shifts is chosen to move the $\langle X_{\rm max} \rangle$ in the same direction as energy. The $\pm 10\,{\rm g\,cm^{-2}}$ in this case is attributed to detector acceptance bias and to reconstruction bias introduced by Cherenkov light modeling (Abbasi et al. 2018a).

The systematics bands displayed in the primary fractions obtained by fitting the data $X_{\rm max}$ distributions were calculated by repeating the fitting procedure with some variations: (1) shift the calorimetric energy of the data by $\pm 10\%$. (2) Shift the MC $X_{\rm max}$ distributions by $\pm 10\,{\rm g\,cm^{-2}}$; a common shift is applied for the four components. (3) Combine these shifts when they have an additive effect on the resulting shift in the fit fractions for the different primaries. We examined six different sets of fits and set the bounds on each primary fraction at the minimum and maximum values obtained by any of the six shifted sets.

We can summarize a set of four fit fractions as a single number using the definition $\langle \ln(A) \rangle = \sum_{ip} f_{ip} \times \ln(A_{ip})$ where ip stands for one of {H, He, N, Fe}. In the following discussion, we use this quantity to examine the overall systematic uncertainty of the composition measurement. We start with Figure 11, showing the six different combinations of energy and $X_{\rm max}$ shifts, discussed above, along with the overall systematics band.

To estimate the size of the uncertainty due to acceptance, we divide the data into multiple subsets and redo the analysis on

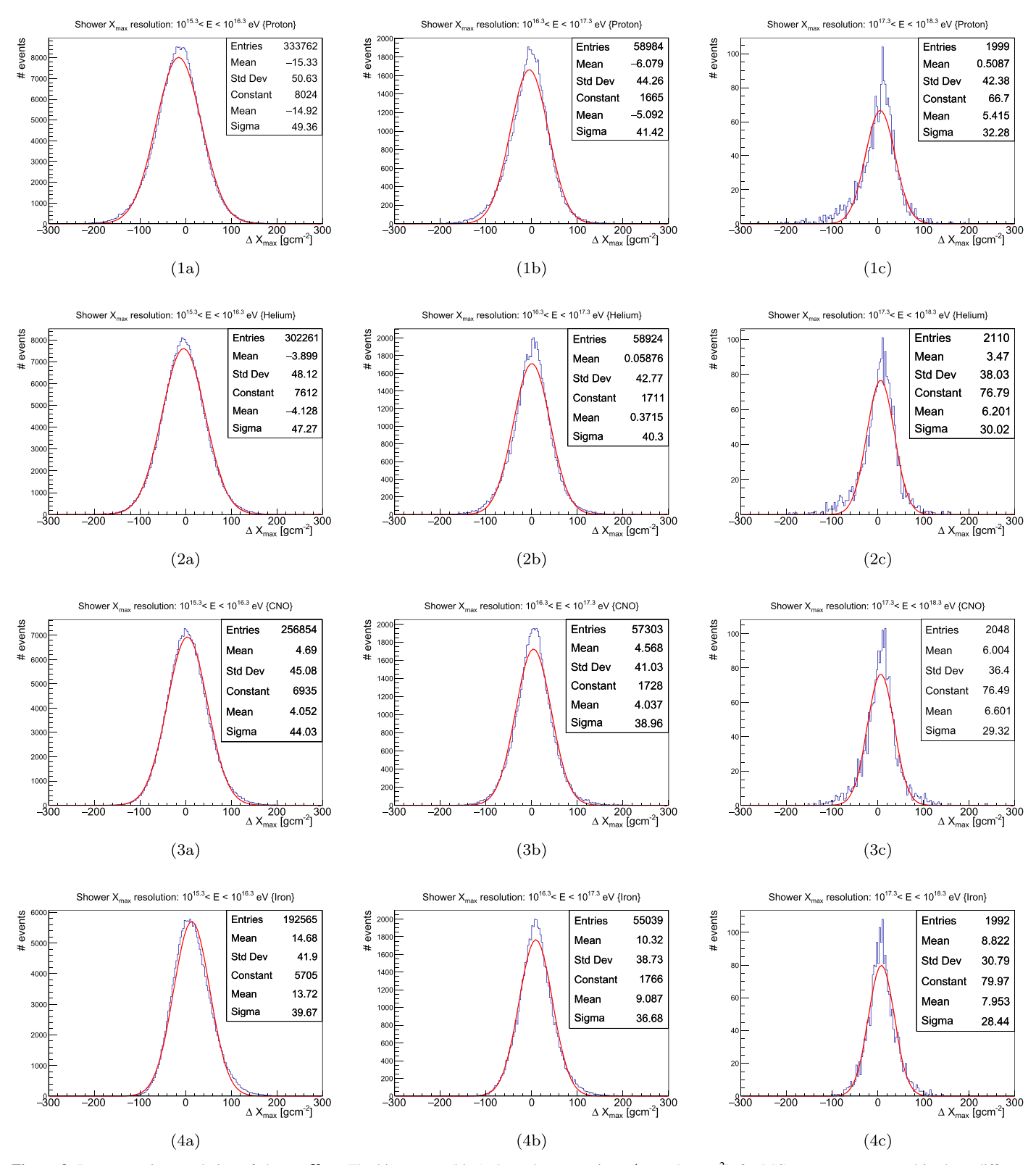


Figure 8. Reconstruction resolution of shower X_{max} . The histograms (blue) show the uncertainty, ΔX_{max} [g cm⁻²], for MC events reconstructed in three different energy ranges: from left to right, (a) $10^{15.3}$ – $10^{16.3}$ eV, (b) $10^{16.3}$ – $10^{17.3}$ eV, and (c) $10^{17.3}$ – $10^{18.3}$ eV. The red curve represents a Gaussian fit to the histogram. The distributions are shown for each of the four simulated primaries: from top to bottom, (1) H, (2) He, (3) N, (4) Fe.

these subsets. We also vary some of the event quality cuts and examine how the results change with these modifications.

The vast majority of the events in the final data set are single-telescope events. Thus, a possible way to create subsets of the data is to divide the set by telescope. "Ring 4" telescopes

view higher elevation angles $(45^{\circ}-59^{\circ})$, therefore they are more likely to trigger on heavy primaries, owing to a shorter path through the atmosphere, than "Ring 3" telescopes (viewing $31^{\circ}-45^{\circ}$ elevation). Division by telescope "ring" is related to division by shower zenith angle, since Cherenkov-dominated

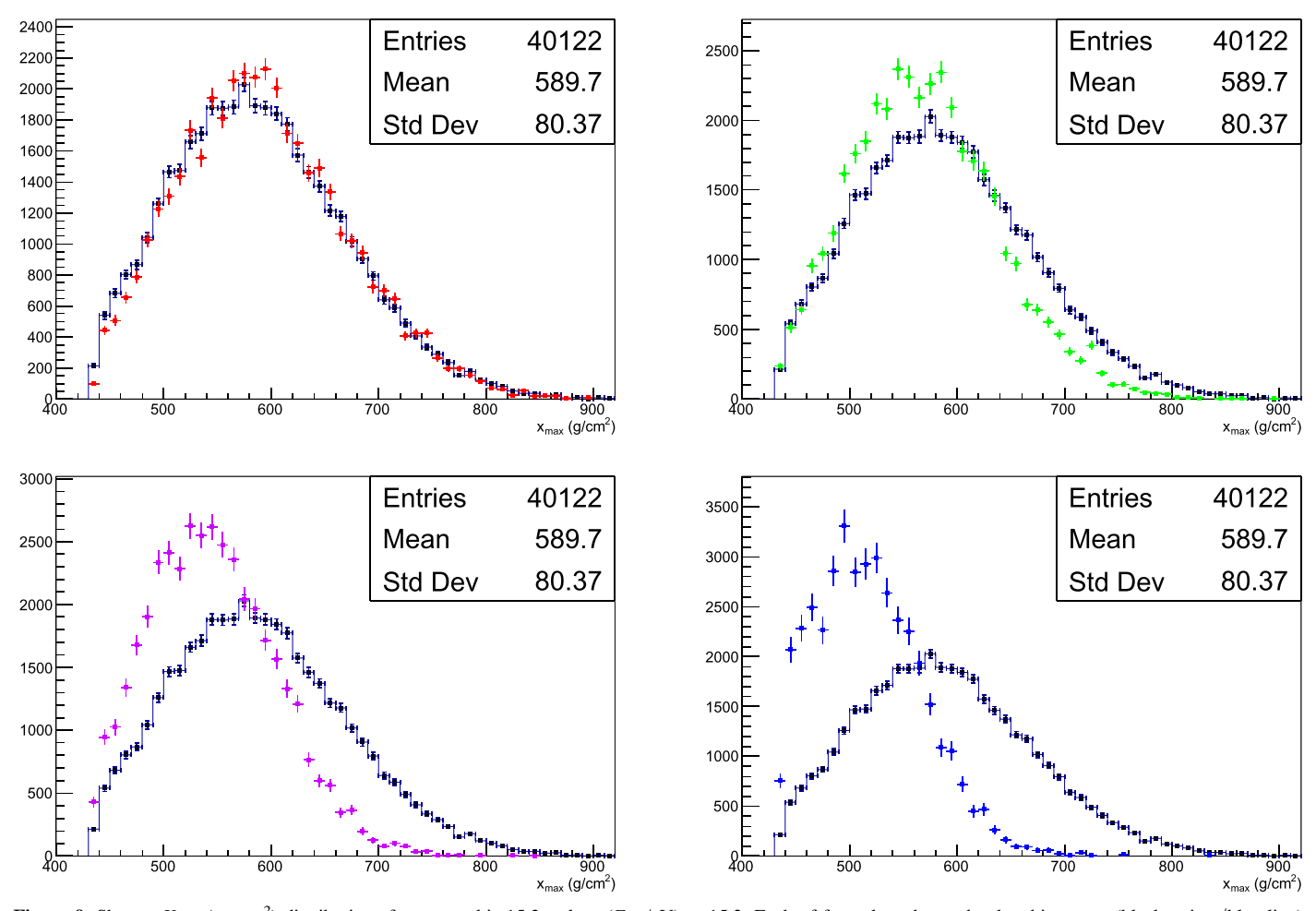


Figure 9. Shower X_{max} (g cm⁻²) distributions for energy bin 15.2 < $\log_{10}(E_{\text{cal}}/\text{eV})$ < 15.3. Each of four plots shows the data histogram (black points/blue line), along with X_{max} reconstructed from MC primaries: upper left plot H (red), upper right He (green), lower left CNO (violet), and lower right Fe (blue).

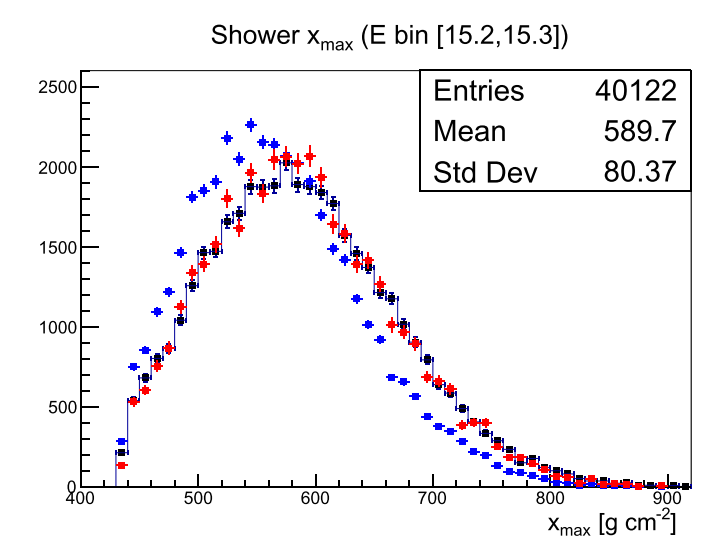


Figure 10. Shower $X_{\rm max}$ (g cm⁻²) distributions for energy bin 15.2 < $\log_{10}(E_{\rm cal}/{\rm eV}) < 15.3$. Black points represent the data; the result of the $X_{\rm max}$ distribution fit (TXF) is shown in red. Using the H4a (Gaisser 2012) composition model as input to the TALE detector MC results in the distribution shown in blue.

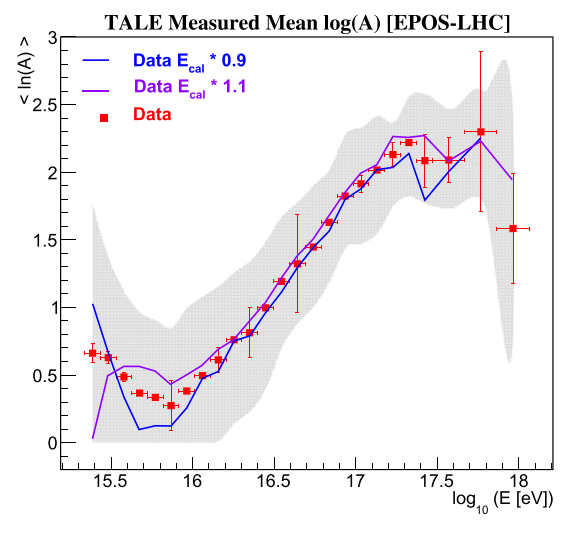
events must have a direction that is close to the pointing angle of the observing telescope. The comparison of the two is shown in Figure 12. As can be seen in the figure, the difference

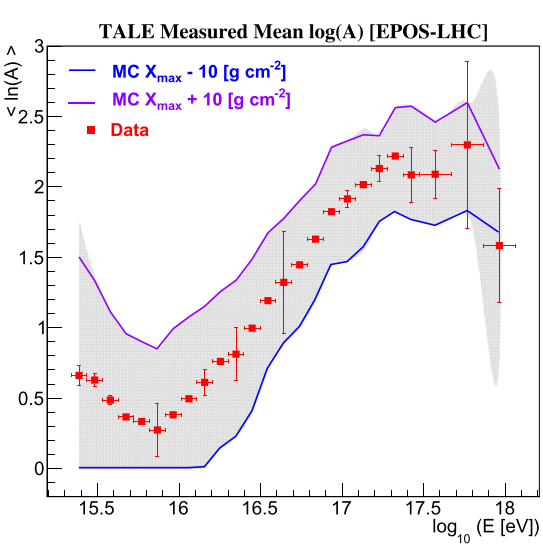
between the two subsets is small relative to other systematics for most of the energy range. Near the ends of the energy range the difference is comparable to other systematics.

An east/west division of telescopes, with the central two telescopes included in both sets, checks for any geomagnetic effect and different sky noise background. Results of a comparison are shown in Figure 13. As can be seen in the figure, there is a relatively small azimuthal effect at higher energies, but it is not a major contributor to the overall systematic uncertainty.

Another source of uncertainty on detector acceptance are time-dependent effects such as atmospheric clarity or sky noise background that may not be accurately reflected in the detector simulation. To examine these effects, we divide the data in time, namely in time of year. Winter months usually allow for longer run periods, and so we divided the data into a set collected during the months of October through February, and another from March through September. This division showed the largest difference in the absolute value of $\langle \ln(A) \rangle$ of all the various checks we performed. The comparison is shown in Figure 14. Despite the use of hourly GDAS atmospheric pressure profiles in the simulation and event reconstruction, we still find a significant difference in the predictions based on season.

A possible cause of the difference is the seasonal variation in the average concentration of atmospheric aerosols. The density of aerosols varies nightly, or even hourly, and it is difficult to





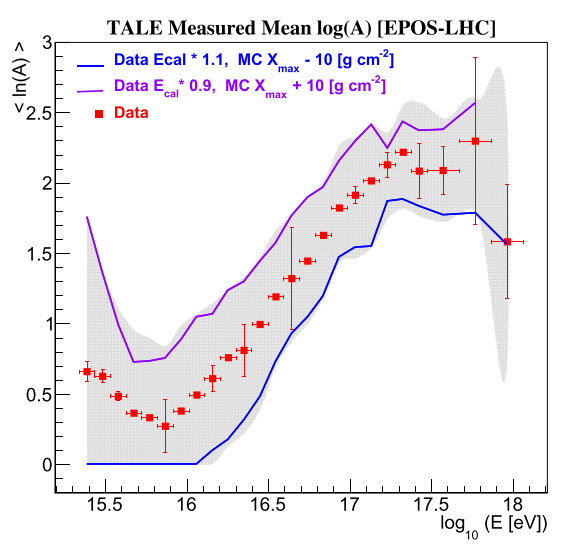


Figure 11. The $\langle \ln(A) \rangle$ systematics band (shown in gray) compared to the effect on the estimated $\langle \ln(A) \rangle$ of shifting the reconstructed data events energy by $\pm 10\%$ (top), or shifting reconstructed $X_{\rm max}$ values of MC showers by $\pm 10~{\rm g~cm^{-2}}$ (middle), or the combination of the two (bottom). In all three panels, points with error bars are TALE data with no systematic shifts to event energy or MC showers $X_{\rm max}$.

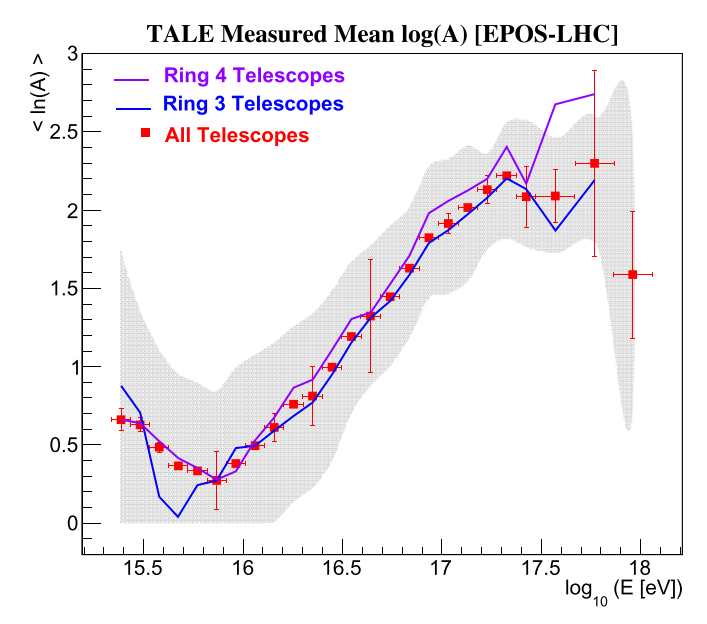


Figure 12. $\langle \ln(A) \rangle$ for the full TALE data set compared to subsets using Ring 3 (31°-45° elevation) and Ring 4 (45°-59° elevation) events separately. For most of the energy range, the difference between the two subsets is small relative to other systematics. Near the bottom and top of the energy range the difference is comparable to other systematics.

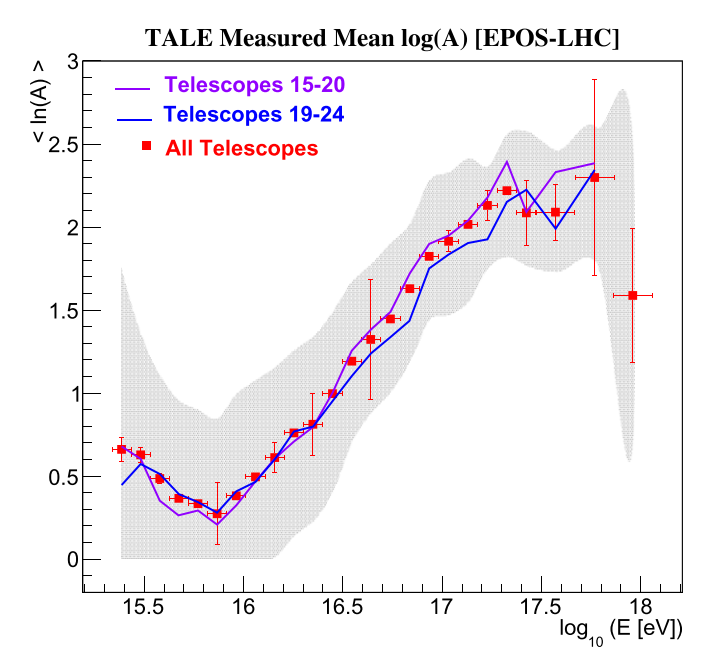


Figure 13. $\langle \ln(A) \rangle$ for the full TALE data set compared to subsets using telescopes with different azimuthal viewing directions. Telescopes 15–20 point farther east, while 19–24 point farther west; telescopes 19 and 20 are shared by the two subsets. As can be seen in the plot, there is a relatively small azimuthal effect at higher energies, but it is not a major contributor to the overall systematic uncertainty.

measure continuously. It can be treated on average however. For the TALE analysis, an average concentration characterized by the *vertical aerosols optical depth*, VAOD, is used. Aerosols attenuate the light signal reaching the detector from the shower. Therefore, a variation in the concentration of aerosols results in a variation in the amount of light reaching the detector from the shower. An increase in the light

TALE Measured Mean log(A) [EPOS-LHC] Months Oct - Feb Months Mar - Sep All Months 2 1.5 15.5 16 16.5 17 17.5 18 log₁₀ (E [eV])

Figure 14. $\langle \ln(A) \rangle$ for the full TALE data set compared to subsets using "winter" months October through February and the months of March through September. This breakdown gives similar number of events in each subset. Despite the use of hourly GDAS atmospheric pressure profiles in the simulation and event reconstruction, we still find a significant difference in the predictions based on season.

attenuation can cause some showers to either fail to trigger the detector or else to pass some reconstruction or quality cut. Summer months in Utah tend to have poorer air quality, i.e., more aerosols, and therefore more light attenuation. Showers created by heavier primaries, larger $\ln(A)$, develop higher up in the atmosphere, and light produced by these showers will travel further in the atmosphere, through more aerosols, to reach the detector. We speculate that the effect of increased average concentration of aerosols will be stronger for heavier primaries than light primaries, resulting in a decrease in the fraction of heavy primaries in the data and therefore smaller $\langle \ln(A) \rangle$. This is the observed effect for TALE, as can be seen in Figure 14.

Another approach to look at time dependence of the result is to use the bootstrap method (Efron 1979) to sample different run months and form a data set comparable to the actual set in terms of the number of events. The complete observation period comprises 58 run months. By sampling run months instead of individual events, we maintain the correspondence between the simulation and real data included in the sampled set. We performed 37 iterations to obtain a measure of the stability of the result and to get a sense of the expected spread of the result due to inclusion or exclusion of certain run periods. Results are shown in Figure 15. By randomly sampling the run months we get a measure of the overall effect of atmospheric variation on the composition result. We see that, when averaged over the entire data set, the effect of atmospheric variations on the composition result is likely smaller than the expectation based on the seasons, shown in Figure 14.

Finally, we examined varying some of the quality cuts applied to the data and simulation sets. As an example, the effect of changing the cut value of the angular track-length is shown in Figure 16. As can be seen in the figure, changing the cut in track-length has a minimal effect on the composition

results. Similar results were observed for other cut parameters examined as part of the data analysis.

7. Results and Discussion

We present the results of the analysis in the following forms.

- 1. Measured $\langle X_{\rm max} \rangle$ evolution with shower energy. These values are for the final event sample and do not include corrections for detector acceptance bias or other biases related to event selection or event reconstruction. We also show the results for reconstructed MC showers for comparison with the data.
- 2. Estimated cosmic-ray primary fractions based on the full measured $X_{\rm max}$ distribution, using a four-component fit. The primary fractions in this case are corrected for biases in detector acceptance, event selection, and event reconstruction.
- 3. Resulting $\langle \ln(A) \rangle$ from the bias-corrected four-component fit. This result can be thought of as a condensed form of the four-component fit result.
- 4. Bias-corrected X_{max} using EPOS-LHC fit fractions and the unbiased EPOS-LHC MC prediction for the mean X_{max} of the four primary particles used in the analysis.

Where applicable, the above results are shown separately for the two hadronic models, QGSJetII-03 and EPOS-LHC.

Figure 17 shows the mean X_{max} values of TALE data along with those of simulated showers. At $\sim 10^{18}$ eV, it can be seen that the event statistics becomes low. The data are presented in Tables 3 and 4 in the Appendix.

The elongation rate at energies below $10^{17.3}$ eV indicates that the composition is getting heavier in this energy range. A change in the elongation rate (slope of the line fit to $X_{\rm max}$ versus energy) is clearly seen for energies greater than 10^{17} eV that is not present in the MC showers for any one primary type. This change in slope can be interpreted as a change in composition. A broken line fit (one floating break point) to the slope is used to determine the energy at which the slope changes. The fit is shown in Figure 18; fit results are presented in Table 2. The fit line is in agreement with the mean $X_{\rm max}$ values measured by the Telescope Array detectors at EeV energies (Abbasi et al. 2018b), as can be seen in Figure 18.

Data X_{max} distributions were created for each energy bin, using a bin width of 0.1 in $\log_{10}(E)$ up to an energy of $10^{17.4}$ eV, then 0.2 in $\log E$ up to 10^{18} eV. These distributions were fit using MC distributions created using either of two hadronic interaction models, and containing four different primaries. Fit results are shown in Figure 19. The small number of observed events with energies greater than 10¹⁸ eV was not sufficient to extend the fits beyond 10^{18} eV. Figure 19 shows that the proton fraction is dominant at energies below $\sim 10^{16}$ eV. Only a small contribution from iron is seen, and helium and CNO fractions are too small to measure. The helium fraction only becomes appreciable at an energy $\sim 10^{16}$ eV, and is followed by contributions from CNO and iron at higher energies as expected (Peters 1961). The observed dominance of protons at energies below $\sim 10^{16}$ eV is in contrast with recent observations by IceTop (Abbasi et al. 2013) and IceCube (Aartsen et al. 2017), which report a more even mixture of the four components, (H, He, O, Fe), as shown in Figure 15 of Aartsen et al. (2019). KASCADE (Antoni et al. 2003), on the other hand, seems to favor a dominant role for helium over protons in this energy region (Antoni et al. 2005). Extrapolation of lower-energy

TALE Measured Mean log(A) [EPOS-LHC]

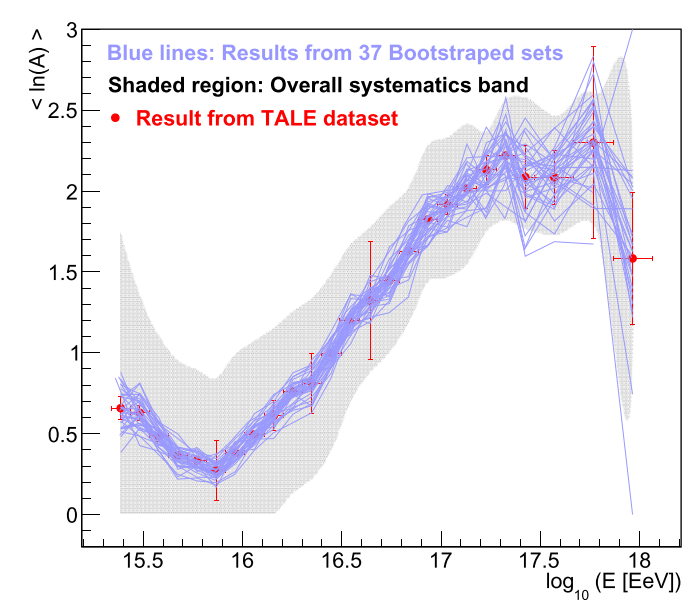


Figure 15. $\langle \ln(A) \rangle$ for the full TALE data set compared to 37 artificial sets generated using the bootstrap method, with sampling over run months (58 months in total). By randomly sampling the run months we get a measure of the overall effect of atmospheric variation on the composition result. We see that, when averaged over the entire data set, the effect of atmospheric variations on the composition result is likely smaller than the expectation based on the seasons, shown in Figure 14.

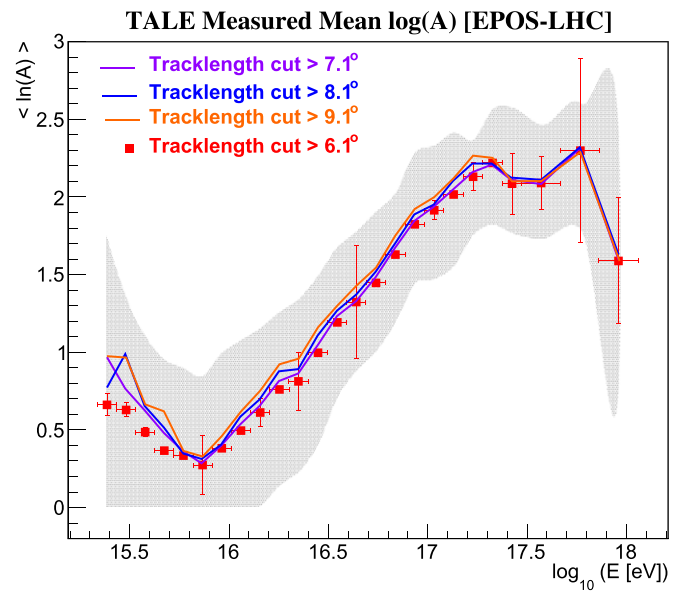
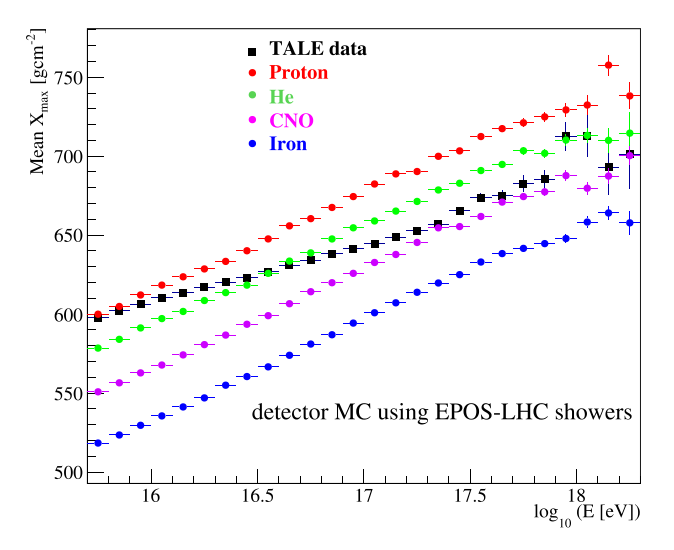


Figure 16. $\langle \ln(A) \rangle$ for TALE data using standard quality cuts compared to changes of cut value on the event angular track-length. As can be seen, changing the cut in track-length has a minimal effect on the composition results. Similar results were observed for other cut parameters examined as part of the data analysis.

measurements by CREAM (Yoon et al. 2017) also leads to the expectation that the helium contribution should be comparable to, if not larger than, that of protons at TALE observed energies below $\sim 10^{16}$ eV.

Due to the significant overlap of the proton and helium X_{max} distributions, and the dependence of the predicted distributions on the hadronic model, it is possible that some of the helium

TALE Reconstructed Shower X_{max} vs Reconstructed Shower Energy



TALE Reconstructed Shower X_{max} vs Reconstructed Shower Energy

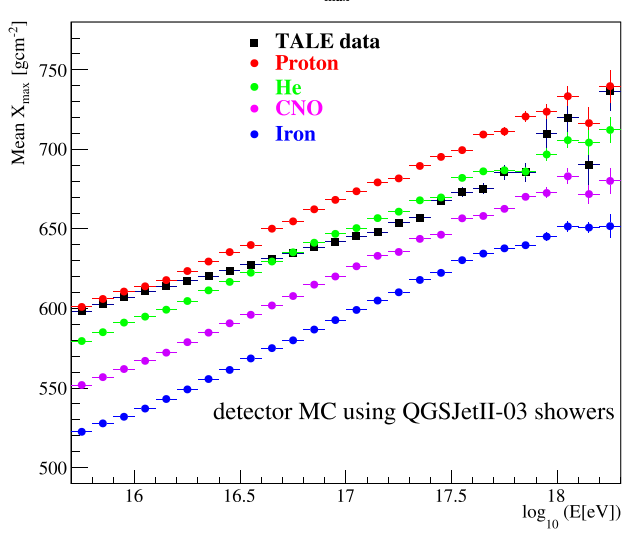
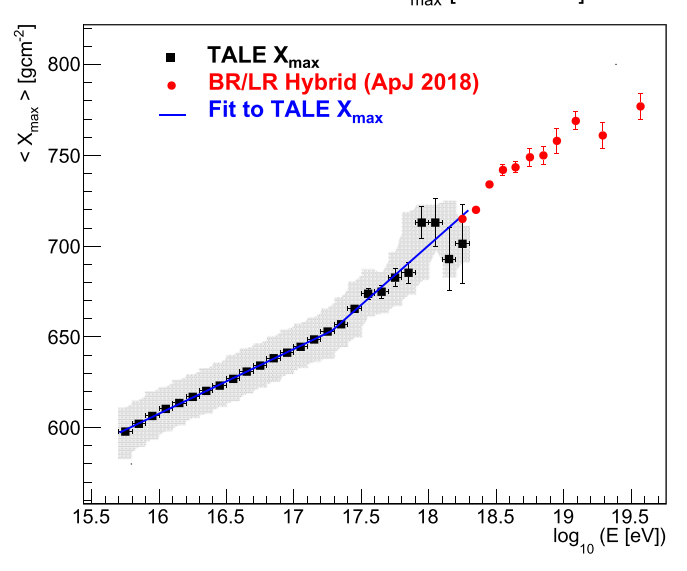


Figure 17. Mean $X_{\rm max}$ as a function of energy for the reconstructed TALE events. The estimate of shower missing-energy correction using EPOS-LHC is shown in the upper plot, and that using QGSJetII-03 in the lower plot. The reconstructed $X_{\rm max}$ values for the four MC primaries, generated and reconstructed using the corresponding hadronic model, are shown alongside the data for comparison. The composition appear to be getting heavier with energy in this range for both models.

contribution to the CR flux is getting misidentified as proton contribution. We studied the event reconstruction performance and the systematic uncertainties of the measurement to estimate the size of this effect. In addition to the reconstruction performance and systematics studies discussed above, additional checks were made to test the proton fraction for the lower-energy bins. The fit to the full $X_{\rm max}$ distributions was modified in two ways. First, the range of accepted shower $X_{\rm max}$ was restricted to values less than 760 g cm⁻² (compare to Figure 10). This should cut any bias on the fit result due to the tail of the distribution, which is expected to be all protons. This change resulted in an insignificant change to the fit result for all energy bins below $\sim 10^{16}$ eV. Second, in a separate check, the recorded proton fit fraction was constrained to be smaller than 80%. In this case, as expected, the fitter set the proton fit fraction "at the limit," i.e., 80%, and increased the helium fit

TALE Measured Shower X_{max} [EPOS-LHC]



TALE Measured Shower X_{max} [QGSJetII-03]

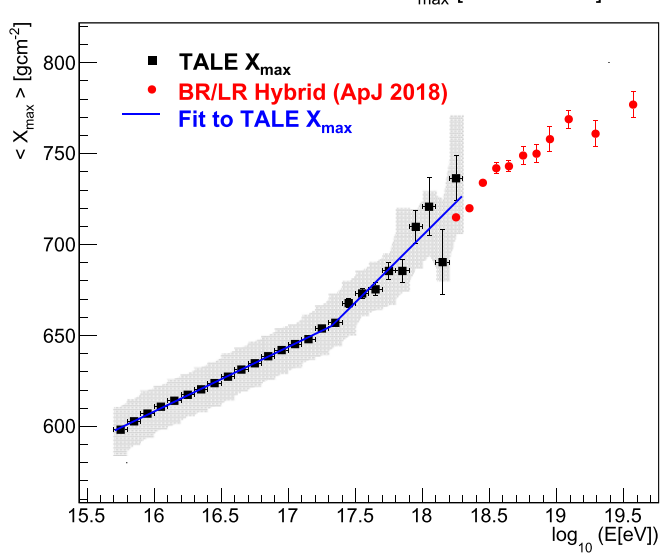


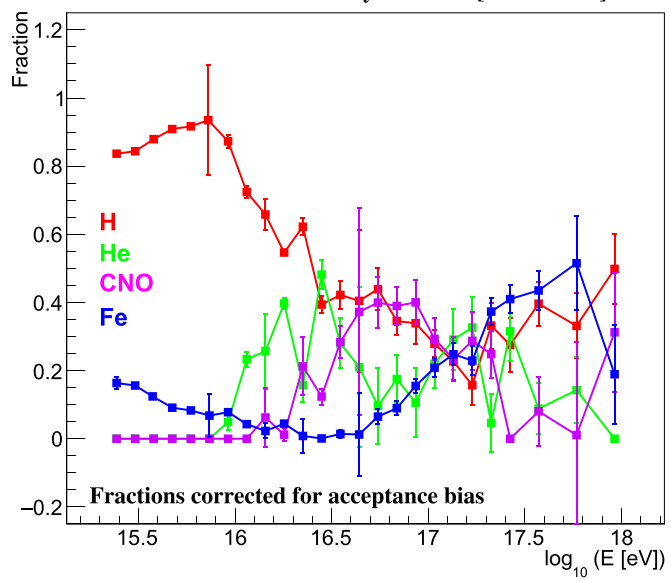
Figure 18. Mean X_{max} as a function of energy for the reconstructed TALE events. The estimate of shower missing-energy correction using EPOS-LHC is shown in the upper plot, and that using QGSJetII-03 in the lower plot. A broken line fit is shown for each plot. Fit parameters are listed in Table 2. Red points at higher energies come from a hybrid measurement by the main Telescope Array telescopes (Abbasi et al. 2018b).

Table 2
Fit Parameters to a Broken Line Fit to TALE $X_{\rm max}$ Elongation Rate Break-point Energies are Expressed as $\log_{10}(E/eV)$, and the Slopes Have Units of $(gcm^{-2})/decade$

EPOS-LHC	Break point Slope before Slope after	$17.291 \pm 0.060 + 0.077 - 0.084$ $35.863 \pm 0.294 + 1.481 - 0.536$ $65.413 \pm 6.655 + 0.000 - 3.269$
QGSJetII-03	Break point Slope before Slope after	$17.310 \pm 0.049 + 0.052 - 0.179$ $35.784 \pm 0.298 + 1.337 - 0.667$ $70.860 \pm 6.508 + 0.000 - 11.387$

Note. Break-point energies are expressed as $\log_{10}(E/\text{eV})$, and the slopes have units of (g cm⁻²)/decade. Uncertainties are reported as value $\pm \sigma_{\text{stat.}} + \sigma_{\text{sys.}} - \sigma_{\text{sys.}}$.

TALE Measured Primary Fractions [EPOS-LHC]



TALE Data: Primary Fractions [QGSJetII-03]

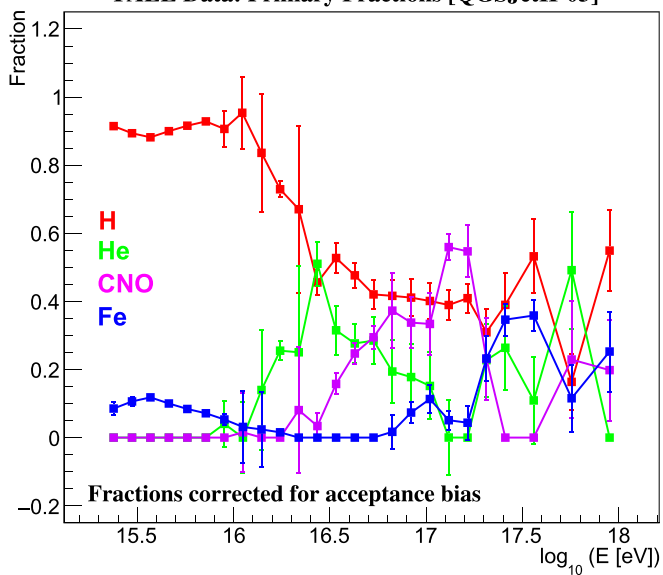


Figure 19. Estimated primary CR fractions based on a fit of the data $X_{\rm max}$ distribution to a weighted sum of $X_{\rm max}$ distributions from a four-component MC simulation. A best match to the data distribution results when the MC primaries are combined with weights equal to the shown fractions. One fit is performed for each energy bin. Primary fractions using the EPOS-LHC based simulations are shown in the top plot, those using QGSJetII-03 in the bottom plot.

fraction to compensate for the missing protons. For most low-energy bins, the resulting fit χ^2 was larger by roughly 3σ than the $\chi^2_{\rm min}$ obtained for the unconstrained fit. The fit quality got worse for smaller proton fraction limits.

Resolving the proton and helium components of the CR flux may have involved some subtle effects that escaped our scrutiny. One can take a more conservative viewpoint, and treat the combined proton and helium fractions as representing the "light" component of the cosmic-ray flux. However, we present the fit results for the individual primaries, along with estimated systematic uncertainties, as our best estimate of the primary fractions in the CR flux.

log₁₀ (E [eV])

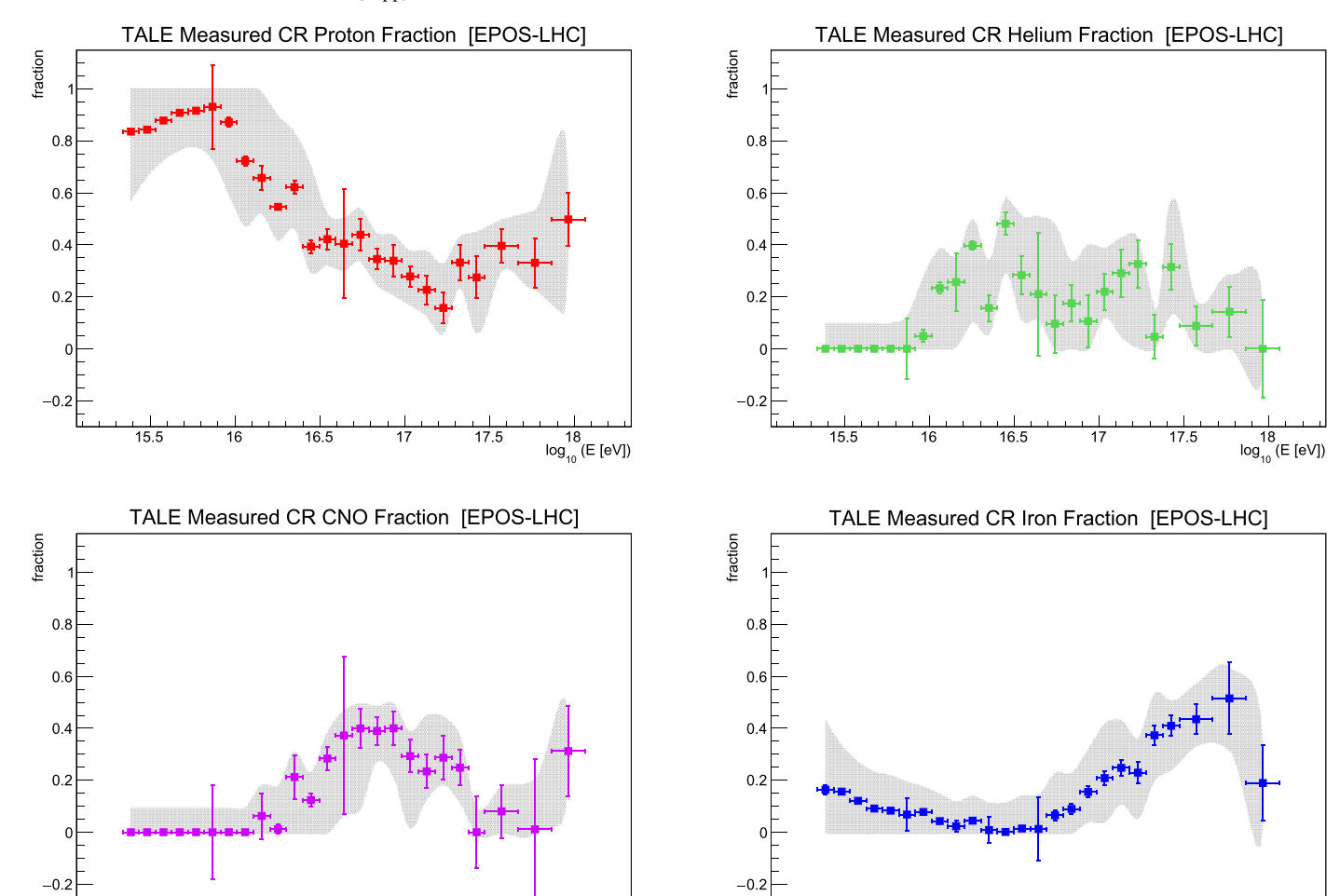


Figure 20. Primary fractions using the EPOS-LHC based simulations are shown for a four-primary composition.

18 log₁₀ (E [eV])

To incorporate the systematic uncertainty into the presentation of the results we focus our attention on the EPOS-LHC based analysis. The primary fractions are shown separately in Figure 20, followed by the estimated $\langle \ln(A) \rangle$ displayed in Figure 21. Similar to the trend found for $\langle X_{\rm max} \rangle$, Figures 20 and 21 also indicate that the composition is getting heavier in the $10^{16}\,{\rm eV}$ decade, and that there is a further change just above $10^{17}\,{\rm eV}$.

Finally, similar to the calculation of $\langle \ln(A) \rangle$, the biascorrected fractions were used to calculate a no-bias $\langle X_{\rm max} \rangle = \sum_{ip} f_{ip} \times \langle X_{\rm max}^{(ip)} \rangle$, where ip stands for one of {H, He, N, Fe}, and $\langle X_{\rm max}^{(ip)} \rangle$ is the EPOS-LHC predicted (MC thrown) $\langle X_{\rm max} \rangle$ of primary ip. These results are displayed in Figure 22, with data in Table 5.

8. Summary

We have presented the results of a measurement of the cosmic-ray composition in the energy range $10^{15.3}$ – $10^{18.3}$ eV using data collected by the TALE detector over a period of roughly four years. An examination of the mean $X_{\rm max}$ versus energy (Figures 17, 18) shows a composition that is getting heavier, followed by a change in the $X_{\rm max}$ elongation rate at an energy of $\sim 10^{17.3}$ eV. This "break" in the elongation rate is likely correlated with the observed break in the cosmic-ray energy spectrum (Abbasi et al. 2018a).

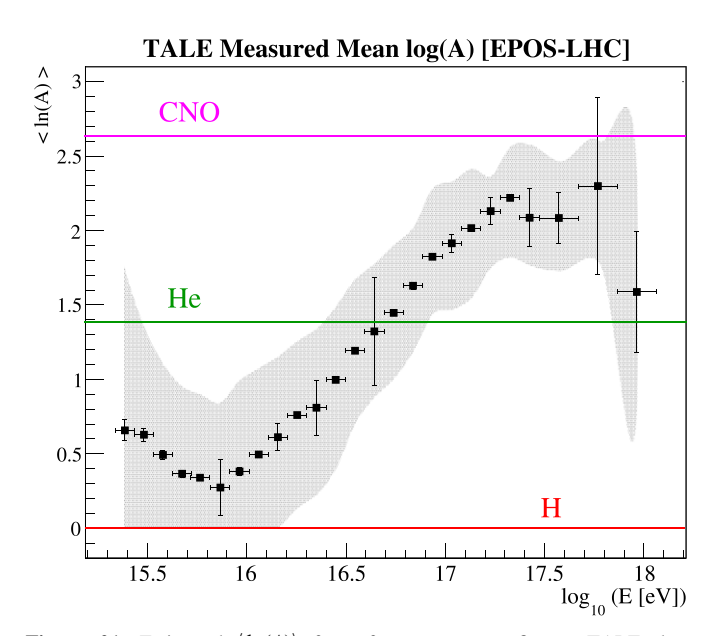


Figure 21. Estimated $\langle \ln(A) \rangle$ from four-component fits to TALE data. Horizontal lines show calculated $\ln(A)$ values for H, He, and N, for reference.

We also fit the data X_{max} distributions, per energy bin, to reconstructed MC showers generated for four primary particle types. These fits show a light composition of mostly protons

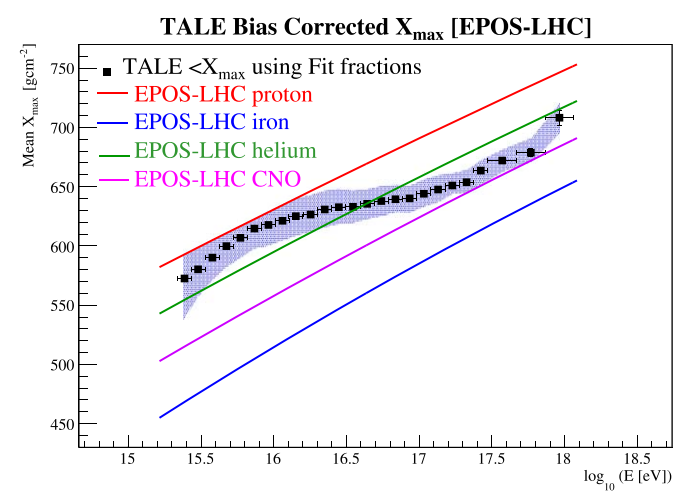


Figure 22. Bias-corrected $X_{\rm max}$ using EPOS-LHC fit fractions and the unbiased EPOS-LHC MC prediction for the mean $X_{\rm max}$ of the four primary particles used in the analysis. These results include a first-order correction to the detector acceptance bias.

and helium at the lower energies, becoming more mixed near 10^{17} eV. In this analysis, we do not have sufficient statistics to comment on the composition for cosmic rays with energies greater than 10^{18} eV. These results are shown as the fractions themselves (Figures 19, 20), as a derived mean $\ln(A)$ (Figure 21), and as a derived mean X_{max} (Figure 22).

The Telescope Array experiment is supported by the Japan Society for the Promotion of Science (JSPS) through Grants-in-Aid for Priority Area 431, for Specially Promoted Research JP21000002, for Scientific Research (S) JP19104006, for Specially Promoted Research JP15H05693, for Scientific Research (S) JP15H05741, for Science Research (A) JP18H03705, for Young Scientists (A) JPH26707011, and for Fostering Joint International Research (B) JP19KK0074, by the joint research program of the Institute for Cosmic Ray Research (ICRR), The University of Tokyo; by the Pioneering Program of

RIKEN for Matter in the Universe (r-EMU); by the U.S. National Science Foundation awards PHY-1404495, PHY-1404502, PHY-1607727, PHY-1712517, and PHY-1806797; by the National Research Foundation of Korea (2017K1A4A3015188. 2020R1A2C1008230, & 2020R1A2C2102800); by the Russian Science Foundation grant 20-42-09010 (INR), IISN project No. 4.4501.18, and Belgian Science Policy under IUAP VII/37 (ULB). The foundations of Dr. Ezekiel R. and Edna Wattis Dumke, Willard L. Eccles, and George S. and Dolores Doré Eccles all helped with generous donations. The State of Utah supported the project through its Economic Development Board, and the University of Utah through the Office of the Vice President for Research. The experimental site became available through the cooperation of the Utah School and Institutional Trust Lands Administration (SITLA), U.S. Bureau of Land Management (BLM), and the U.S. Air Force. We appreciate the assistance of the State of Utah and Fillmore offices of the BLM in crafting the Plan of Development for the site. Patrick A. Shea assisted the collaboration with valuable advice and supported the collaboration's efforts. The people and the officials of Millard County, Utah have been a source of steadfast and warm support for our work, which we greatly appreciate. We are indebted to the Millard County Road Department for their efforts to maintain and clear the roads that get us to our sites. We gratefully acknowledge the contribution from the technical staffs of our home institutions. An allocation of computer time from the Center for High Performance Computing at the University of Utah is gratefully acknowledged.

Software: CONEX (Bergmann et al. 2007), CORSIKA (Heck et al. 1998), CORSIKA/IACT (Bernlohr 2008).

Appendix

Mean shower $X_{\rm max}$ for events included in the composition analysis of TALE data are shown in Tables 3 and 4. The number of events in each energy bin, along with $X_{\rm max}$ and the estimated errors are listed. Table 5 lists the bias-corrected $\langle X_{\rm max} \rangle$ of data events, estimated using the bias-corrected fit fractions from EPOS-LHC based analysis.

Table 3 $\langle X_{\text{max}} \rangle$ of Data Events

Table 4 $\langle X_{\text{max}} \rangle$ of Data Events

Energy Bin	Number	$\langle X_{\rm max} \rangle \pm \sigma_{\rm stat.} + / - \sigma_{\rm sys.}$	Energy Bin	Number	$\langle X_{\rm max} \rangle \pm \sigma_{\rm stat.} + / - \sigma_{\rm sys.}$
$\log_{10}(E/\text{eV})$	of Events	$(g cm^{-2})$	$\log_{10}(E/\text{eV})$	of Events	$(g cm^{-2})$
15.30–15.40	39,669	$590.1 \pm 0.4 + 10.0 - 10.0$	15.30–15.40	43,977	$589.3 \pm 0.4 + 10.0 - 10.0$
15.40-15.50	71,699	$585.8 \pm 0.3 + 10.0 - 10.0$	15.40-15.50	75,692	$585.6 \pm 0.3 + 10.0 - 10.0$
15.50-15.60	98,113	$585.8 \pm 0.3 + 12.4 - 10.5$	15.50-15.60	100,698	$586.1 \pm 0.3 + 13.0 - 10.8$
15.60-15.70	109,055	$589.8 \pm 0.2 + 15.6 - 12.8$	15.60-15.70	109,617	$590.8 \pm 0.2 + 15.3 - 13.3$
15.70-15.80	97,017	$597.9 \pm 0.3 + 13.0 - 14.9$	15.70-15.80	96,990	$598.2 \pm 0.3 + 13.3 - 14.4$
15.80-15.90	91,380	$602.1 \pm 0.3 + 12.8 - 12.6$	15.80-15.90	89,810	$602.8 \pm 0.3 + 12.8 - 12.6$
15.90-16.00	78,444	$606.4 \pm 0.3 + 13.2 - 12.7$	15.90-16.00	76,271	$607.0 \pm 0.3 + 13.2 - 12.9$
16.00-16.10	64,594	$610.4 \pm 0.3 + 12.0 - 12.2$	16.00-16.10	62,828	$610.8 \pm 0.3 + 12.1 - 11.8$
16.10-16.20	51,230	$613.6 \pm 0.3 + 12.7 - 12.2$	16.10-16.20	49,683	$614.1 \pm 0.3 + 12.4 - 12.5$
16.20-16.30	40,036	$617.0 \pm 0.4 + 12.2 - 11.5$	16.20-16.30	38,534	$617.4 \pm 0.4 + 12.1 - 11.4$
16.30-16.40	30,915	$620.3 \pm 0.4 + 12.1 - 12.5$	16.30-16.40	29,904	$620.4 \pm 0.4 + 12.5 - 11.8$
16.40-16.50	23,657	$623.2 \pm 0.4 + 12.4 - 11.7$	16.40-16.50	22,732	$623.8 \pm 0.4 + 12.1 - 12.1$
16.50-16.60	17,972	$626.9 \pm 0.5 + 13.1 - 12.2$	16.50-16.60	17,201	$627.3 \pm 0.5 + 13.2 - 12.4$
16.60-16.70	13,517	$630.9 \pm 0.6 + 12.7 - 12.2$	16.60-16.70	13,166	$631.3 \pm 0.6 + 12.5 - 11.7$
16.70-16.80	9940	$634.2 \pm 0.6 + 12.2 - 12.1$	16.70-16.80	9447	$634.7 \pm 0.7 + 12.7 - 12.3$
16.80-16.90	7644	$638.3 \pm 0.7 + 11.8 - 12.8$	16.80-16.90	7338	$638.6 \pm 0.8 + 11.8 - 12.4$
16.90-17.00	5560	$641.3 \pm 0.8 + 12.8 - 11.9$	16.90-17.00	5389	$642.0 \pm 0.9 + 12.8 - 12.6$
17.00-17.10	4284	$644.5 \pm 1.0 + 12.9 - 11.5$	17.00-17.10	4075	$645.3 \pm 1.0 + 11.4 - 12.4$
17.10-17.20	3059	$648.6 \pm 1.1 + 12.0 - 12.2$	17.10-17.20	2916	$648.0 \pm 1.1 + 14.2 - 10.8$
17.20-17.30	1833	$653.0 \pm 1.4 + 12.8 - 14.8$	17.20-17.30	1719	$653.9 \pm 1.5 + 13.0 - 14.3$
17.30-17.40	1295	$657.0 \pm 1.8 + 14.8 - 12.4$	17.30-17.40	1241	$657.0 \pm 1.8 + 16.4 - 12.3$
17.40-17.50	807	$665.5 \pm 2.2 + 15.1 - 15.9$	17.40-17.50	762	$667.8 \pm 2.4 + 12.6 - 17.5$
17.50-17.60	487	$673.8 \pm 2.9 + 13.4 - 12.5$	17.50-17.60	450	$673.1 \pm 3.0 + 13.2 - 11.8$
17.60-17.70	300	$674.9 \pm 3.6 + 10.6 - 11.9$	17.60-17.70	285	$675.4 \pm 3.6 + 15.5 - 10.8$
17.70-17.80	176	$682.7 \pm 4.9 + 14.0 - 15.6$	17.70-17.80	167	$685.5 \pm 4.9 + 10.0 - 18.5$
17.80-17.90	112	$685.4 \pm 5.7 + 33.4 - 12.0$	17.80-17.90	107	$685.5 \pm 6.1 + 35.0 - 10.9$
17.90-18.00	57	$712.5 \pm 9.0 + 10.0 - 31.4$	17.90-18.00	50	$709.8 \pm 9.2 + 10.0 - 22.7$
18.00-18.10	25	$712.8 \pm 13.4 + 10.0 - 14.8$	18.00-18.10	20	$719.9 \pm 15.9 + 10.0 - 25.6$
18.10-18.20	16	$692.9 \pm 17.4 + 32.2 - 10.0$	18.10-18.20	16	$690.4 \pm 18.0 + 35.0 - 10.0$
18.20-18.30	5	$701.3 \pm 21.8 + 10.0 - 10.0$	18.20-18.30	5	$736.5 \pm 12.3 + 35.0 - 30.4$

Note. Missing-energy correction based on the EPOS-LHC hadronic model.

Note. Missing-energy correction based on the QGSJetII-03 hadronic model.

Bias-corrected $\langle X_{\text{max}} \rangle$ of Data Events, Estimated using the Bias-corrected Fit Fractions from EPOS-LHC Based Analysis

Energy Bin log ₁₀ (E/eV)	Number of Events	$\langle X_{\rm max} \rangle \pm \sigma_{\rm stat.} + /- \sigma_{\rm sys.}$ (g cm ⁻²)
15.338–15.434	40,122	$572.5 \pm 0.4 + 20.4 - 34.0$
15.434-15.530	70,340	$579.6 \pm 0.3 + 19.2 - 22.6$
15.530-15.626	94,914	$590.1 \pm 0.3 + 14.7 - 19.0$
15.626-15.723	105,576	$599.8 \pm 0.2 + 11.0 - 17.7$
15.723-15.819	95,197	$606.8 \pm 0.3 + 9.9 - 16.8$
15.819-15.915	90,591	$614.7 \pm 0.3 + 8.0 - 16.6$
15.915-16.012	78,786	$617.7 \pm 0.3 + 10.9 - 17.1$
16.012-16.109	65,331	$621.2 \pm 0.3 + 13.3 - 16.3$
16.109-16.205	52,467	$624.2 \pm 0.3 + 15.9 - 15.3$
16.205-16.302	41,031	$626.5 \pm 0.3 + 16.2 - 14.1$
16.302-16.399	31,743	$630.8 \pm 0.4 + 15.6 - 14.8$
16.399-16.496	24,609	$632.7 \pm 0.4 + 15.3 - 13.9$
16.496-16.594	18,644	$633.0 \pm 0.5 + 13.4 - 13.3$
16.594-16.691	14,051	$635.5 \pm 0.6 + 12.2 - 12.6$
16.691-16.788	10,544	$637.9 \pm 0.6 + 12.5 - 12.4$
16.788-16.886	7920	$639.4 \pm 0.7 + 12.0 - 11.0$
16.886-16.984	5919	$640.1 \pm 0.8 + 10.6 - 12.0$
16.984-17.081	4485	$644.0 \pm 0.9 + 11.9 - 11.0$
17.081-17.179	3259	$647.6 \pm 1.1 + 11.9 - 10.8$
17.179-17.277	2031	$651.0 \pm 1.3 + 10.1 - 7.0$
17.277-17.375	1377	$653.8 \pm 1.7 + 10.3 - 9.1$
17.375-17.473	904	$663.6 \pm 2.1 + 8.7 - 11.9$
17.473-17.670	896	$672.1 \pm 2.1 + 9.1 - 9.6$
17.670-17.866	331	$678.7 \pm 3.4 + 12.3 - 7.8$
17.866–18.063	110	$708.2 \pm 6.5 + 12.5 - 12.5$

Note. Statistical uncertainties are those on the mean of the corresponding measured data histogram bin. Systematics are calculated based on estimated systematic uncertainties on primary fit fractions.

ORCID iDs

- T. Abu-Zayyad https://orcid.org/0000-0001-5206-4223
- J. W. Belz https://orcid.org/0000-0001-9779-2750
- D. R. Bergman https://orcid.org/0000-0002-4450-7925
- W. Hanlon https://orcid.org/0000-0002-0109-4737
- K. Hibino https://orcid.org/0000-0001-9259-6371
- T. Ishii https://orcid.org/0000-0001-6690-7834
- D. Ivanov https://orcid.org/0000-0002-4420-2830
- K. Kadota https://orcid.org/0000-0001-7672-1945
- S. Kawakami https://orcid.org/0000-0003-3820-7552
- K. Kawata https://orcid.org/0000-0001-6332-2005
- E. Kido https://orcid.org/0000-0001-7278-3049
- Y. Kimura https://orcid.org/0000-0002-2460-3047
- M. Kuznetsov https://orcid.org/0000-0002-8787-0660
- J. P. Lundquist https://orcid.org/0000-0002-4245-5092
- J. N. Matthews https://orcid.org/0000-0001-6940-5637
- K. Mukai https://orcid.org/0000-0002-8286-8094
- R. Nakamura https://orcid.org/0000-0002-2620-9211

- T. Nonaka https://orcid.org/0000-0003-4795-500X
- S. Ogio https://orcid.org/0000-0002-8300-2954
- M. Ono https://orcid.org/0000-0002-0603-918X
- G. I. Rubtsov https://orcid.org/0000-0002-6106-2673
- D. Ryu https://orcid.org/0000-0002-5455-2957
- T. Sako https://orcid.org/0000-0002-7003-6493
- K. Sano https://orcid.org/0000-0002-6468-8532
- P. Sokolsky https://orcid.org/0000-0003-3391-1022
- Y. Tameda https://orcid.org/0000-0001-9750-5440
- S. B. Thomas https://orcid.org/0000-0002-8828-7856
- P. Tinyakov https://orcid.org/0000-0002-0649-6444
- S. Troitsky https://orcid.org/0000-0001-6917-6600
- Y. Tsunesada https://orcid.org/0000-0001-9238-6817

References

```
Aartsen, M., Ackermann, M., Adams, J., et al. 2017, JINST, 12, P03012
Aartsen, M., Ackermann, M., Adams, J., et al. 2019, PhRvD, 100, 082002
Abbasi, R., Abdou, Y., Ackermann, M., et al. 2013, NIMPA, 700, 188
Abbasi, R. U., Abe, M., Abu-Zayyad, T., et al. 2014, ApJL, 790, L21
Abbasi, R. U., Abe, M., Abu-Zayyad, T., et al. 2015, APh, 64, 49
Abbasi, R. U., Abe, M., Abu-Zayyad, T., et al. 2018a, ApJ, 865, 74
Abbasi, R. U., Abe, M., Abu-Zayyad, T., et al. 2018b, ApJ, 858, 76
Abbasi, R. U., Abu-Zayyad, T., Archbold, G., et al. 2005, ApJ, 622, 910
```

Abu-Zayyad, T., Aida, R., Allen, M., et al. 2012, APh, 39, 109

Abu-Zayyad, T., Aida, R., Allen, M., et al. 2013a, NIMPA, A689, 87

Abu-Zayyad, T., Aida, R., Allen, M., et al. 2013b, ApJ, 768, L1 AbuZayyad, T. Z. 2000, PhD Thesis, Univ. Utah

Aloisio, R., Berezinsky, V., & Blasi, P. 2014, JCAP, 1410, 020

Antoni, T., Apel, W. D., Badea, F., et al. 2003, NIMPA, 513, 490 Antoni, T., Apel, W. D., Badea, F., et al. 2005, APh, 24, 1

ARL-NOAA. 2004, dataset: Global Data Assimilation System (GDAS),

https://data.globalchange.gov/dataset/noaa-ncdc-c00379 Barlow, R. J., & Beeston, C. 1993, CoPhC, 77, 219

Bergmann, T., Engel, R., Heck, D., et al. 2007, APh, 26, 420

Bernlohr, K. 2008, APh, 30, 149

Boyer, J. H., Knapp, B. C., Mannel, E. J., & Seman, M. 2002, NIMPA, A482, 457

Efron, B. 1979, AnSta, 7, 1

Engel, R., Riehn, F., Fedynitch, A., Gaisser, T. K., & Stanev, T. 2017, EPJ Veb Conf., 145, 08001

Filthaut, F. 2002, https://root.cern/doc/master/classTFractionFitter.html Gaisser, T. K. 2012, APh, 35, 801

Heck, D., Schatz, G., Thouw, T., Knapp, J., & Capdevielle, J. N. 1998, CORSIKA: A Monte Carlo Code to Simulate Extensive Air Showers, Technical Report FZKA-6019, Research Center Karlsruhe

Ostapchenko, S. 2007, in AIP Conf. Proc. 928, C2CR07: Colliders to Cosmic Rays (Melville, NY: AIP), 118

Ostapchenko, S. 2011, PhRvD, 83, 014018

Peters, B. 1961, Il Nuovo Cimento, 22, 800

Pierog, T. 2018, PoS, ICRC2017, 1100

Pierog, T., Karpenko, I., Katzy, J. M., Yatsenko, E., & Werner, K. 2015, PhRvC, 92, 034906

Sokolsky, P. 2011, NuPhS, 212, 74

Teshima, M., Ohoka, H., Matsubara, Y., et al. 1986, NIMPA, A247, 399

Thomson, G., Sokolsky, P., Jui, C., et al. 2011, in Proc. of the 32nd Int. Cosmic Ray Conf., ICRC 2011 (Beijing: Institute of High Energy Physics), 337

Tokuno, H., Tameda, Y., Takeda, M., et al. 2012, NIMPA, 676, 54

Yoon, Y., Anderson, T., Barrau, A., et al. 2017, ApJ, 839, 5

Zundel, Z. J. 2016, PhD Thesis, Univ. Utah